Journal of Advances in Modeling Earth Systems

RESEARCH ARTICLE
10.1029/2018MS001336

The KPP Boundary Layer Scheme for the Ocean: Revisiting Its Formulation and Benchmarking One-Dimensional Simulations Relative to LES

Luke Van Roekel[1], Alistair J. Adcroft[2], Gokhan Danabasoglu[3], Stephen M. Griffies[2], Brian Kauffman[3], William Large[3], Michael Levy[3], Brandon G. Reichl[2], Todd Ringler[1], and Martin Schmidt[4]

[1]Fluid Dynamics and Solid Mechanics, Los Alamos National Laboratory, Los Alamos, NM, USA, [2]NOAA/Geophysical Fluid Dynamics Laboratory and Princeton University Program in Atmospheric and Oceanic Sciences, Princeton, NJ, USA, [3]Climate and Global Dynamics Laboratory, National Center for Atmospheric Research, Boulder, CO, USA, [4]Leibniz-Institute for Baltic Sea Research, Warnemünde Rostock, Germany

Abstract We evaluate the Community ocean Vertical Mixing project version of the K-profile parameterization (KPP) for modeling upper ocean turbulent mixing. For this purpose, one-dimensional KPP simulations are compared across a suite of oceanographically relevant regimes against horizontally averaged large eddy simulations (LESs). We find the standard configuration of KPP consistent with LES across many forcing regimes, supporting its physical basis. Our evaluation also motivates recommendations for KPP *best practices* within ocean circulation models and identifies areas where further research is warranted. The original treatment of KPP recommends the matching of interior diffusivities and their gradients to the KPP-predicted values computed in the ocean surface boundary layer (OSBL). However, we find that difficulties in representing derivatives of rapidly changing diffusivities near the base of the OSBL can lead to loss of simulation fidelity. To mitigate this difficulty, we propose and evaluate two computationally simpler approaches: (1) match to the internal predicted diffusivity alone and (2) set the KPP diffusivity to 0 at the OSBL base. We find the KPP entrainment buoyancy flux to be sensitive to vertical grid resolution and details of how to diagnose the KPP boundary layer depth. We modify the KPP turbulent shear velocity parameterization to reduce resolution dependence. Additionally, an examination of LES vertical turbulent scalar flux budgets shows that the KPP-parameterized nonlocal tracer flux is incomplete due to the assumption that it solely redistributes the surface tracer flux. This result motivates further studies of the nonlocal flux parameterization.

Key Points:
- The Community ocean Vertical Mixing (CVMix) project version of the K-profile parameterization (KPP) is compared across a suite of oceanographically relevant regimes against large eddy simulations (LESs)
- The standard configuration of KPP is consistent with LES results across many ocean simulations, but some adaptations of KPP are proposed to improve comparisons with LES
- An alternative, computationally simpler, configuration of KPP is proposed to alleviate the need to represent rapidly changing diffusivities near the base of the ocean surface boundary layer

Correspondence to:
L. Van Roekel,
lvanroekel@lanl.gov

Citation:
Van Roekel, L. P., Adcroft, A., Danabasoglu, G., Griffies, S. M., Kauffman, B., Large, W. G., et al. (2018). The KPP boundary layer scheme for the ocean: Revisiting its formulation and benchmarking one-dimensional simulations relative to LES. *Journal of Advances in Modeling Earth Systems*, *10*, 2647–2685. https://doi.org/10.1029/2018MS001336

Received 2 APR 2018
Accepted 20 SEP 2018
Accepted article online 24 SEP 2018
Published online 5 NOV 2018

1. Introduction

The ocean surface boundary layer (OSBL) mediates momentum, heat, and scalar tracer fluxes between the interior ocean and the atmosphere and cryosphere. Consequently, an accurate parameterization of turbulence and the induced vertical mixing in the OSBL is essential for robust model simulations of climate physics and of the abundance and distribution of important biological and chemical quantities. We here study the formulation and behavior of the K-profile parameterization (KPP; Large et al., 1994), LMD94 for use in parameterizing upper ocean turbulent mixing. Our examination reconsiders many of the underlying physical and numerical foundations of KPP, with our study providing an assessment of the scheme under a suite of forcing scenarios and recommendations for best practices in circulation models.

The KPP mixing scheme has been used in a variety of ocean and climate applications. To maintain a controlled examination framework, we focus on one-dimensional vertical mixing and compare KPP simulations with horizontally homogeneous large eddy simulations (LESs). The fidelity of KPP vertical mixing in the presence of horizontal features (e.g., baroclinic fronts; Bachman et al., 2017) is outside our scope.

1.1. The Suite of Ocean Boundary Layer Parameterizations

Boundary layer parameterizations like KPP assume the turbulent mixing is dominated by vertical fluxes. Presently, varying degrees of complexity are used to parameterize these fluxes. Bulk boundary layer models are perhaps the simplest (e.g., Gaspar, 1988; Kraus & Turner, 1967; Niiler, 1977; Price et al., 1986), where ocean properties (tracers and momentum) are assumed to be vertically uniform in the OSBL. The assumption of no

vertical structure within the boundary layer is both the key simplification and the main deficiency of bulk models. Namely, ocean tracers and momentum are not generally uniform vertically, even in the presence of strong vertical mixing. Hence, vertical integration over the depth of the OSBL precludes the simulation of OSBL processes such as the Ekman spiral and boundary layer restratification (but see Hallberg, 2003, for a method to remedy these deficiencies).

Turbulence kinetic energy (TKE) closure (TC) is another widely used framework for parameterizing upper ocean boundary layer mixing (e.g., Canuto et al., 2001, 2007; Harcourt, 2015; Kantha & Clayson, 1994; Umlauf & Burchard, 2005). In most variants of TC, the profiles of eddy diffusivity and viscosity are dependent on the local TKE, which is prognostic (e.g., Kantha & Clayson, 1994; Mellor & Yamada, 1982). Most TC schemes are local in that the turbulent fluxes of tracers and momentum exist only in the presence of nonzero vertical gradients of the mean quantities. Yet in highly convective conditions strong fluxes exist even in the absence of vertical mean gradients. Thus, many TC models are deficient in highly convective conditions. However, a few TC models (e.g., Lappen & Randall, 2001; Soares et al., 2004; Stull, 1993) do include nonlocal mixing effects.

The K-profile parameterization (KPP; LMD94) aims to fill the middle ground between bulk boundary layer models and prognostic TC models. KPP allows for vertical property variations in the OSBL via a specified vertical shape function (O'Brien, 1970). It was also the first OSBL parameterization to include a parameterized nonlocal transport allowing for the existence of vertical turbulent fluxes in the absence of vertical gradients of mixed quantities.

1.2. The CVMix Project

KPP has been implemented in numerous ocean circulation models. In our experience, each implementation makes slightly distinct physical and numerical choices. Sometimes, these implementation choices have unintended consequences that can negatively impact the KPP boundary layer simulation. This situation provided the mandate for our development of KPP within the CVMix project (Griffies et al., 2015) and for the examination of the CVMix implementation in this paper.

The CVMix library is developed as a suite of standardized vertical mixing parameterizations to be implemented in and called by a three-dimensional ocean circulation or *calling* model. Here we test the CVMix implementation of KPP as realized in three distinct calling models: Model for Prediction Across Scales—Ocean (MPAS-O; Ringler et al., 2013), Modular Ocean Model Version 6 (MOM6; Adcroft et al., 2018), and Parallel Ocean Program Version 2 (POP2; Smith et al., 2010) against LES configured with similar depth and surface forcing against. As a part of the CVMix development, we found details of how KPP is implemented in a calling model explain some differences in behavior relative to LMD94, and thus, the intermodel comparison is important for evaluating the integrity of CVMix-KPP.

The CVMix baseline configuration is summarized in Table 1. We have made two changes relative to traditional configurations of KPP (e.g., Danabasoglu et al., 2006). First, the CVMix baseline configuration of KPP (note that throughout the rest of this paper *KPP* will refer to the CVMix implementation for brevity) does not match KPP diffusivity and viscosity gradients to interior parameterizations. Only the diffusivity and viscosity values are matched. Second, for this work we consider a critical Bulk Richardson number of 0.25 instead of 0.3. Our results suggest (e.g., Figure 11) that matching to interior viscosity and diffusivity values alone is an important inclusion for configurations of KPP. However, as our simulations demonstrate minimal sensitivity to the critical Bulk Richardson number, we cannot make a general recommendation to alter this value from the traditional choice. Finally, we note that a Langmuir Turbulence parameterization (Li et al., 2015) is also implemented in CVMix-KPP, but its evaluation is outside our scope.

1.3. An LES Evaluation Framework for OSBL Parameterizations

LESs provide our evaluation framework for the KPP scheme. As configured here, the LES resolves the dominant eddies and parameterizes subgrid turbulence, which is small relative to that realized at resolved scales away from the parameterized surface layer. The LES is forced with horizontally uniform surface fluxes and the output is horizontally and temporally averaged. We compare the LES results to one-dimensional KPP simulations using identical forcing and initialization.

Numerous studies have compared atmospheric boundary layer parameterizations to LES (e.g., Holtslag & Moeng, 1991; Moeng & Sullivan, 1994; Brown, 1996; Ayotte et al., 1996; Noh et al., 2003). However, there are far fewer LES evaluations of ocean boundary layer parameterizations. Many ocean LES comparisons have used similar (and limited) initial conditions and forcing scenarios (e.g., Bachman et al., 2017; McWilliams & Sullivan,

Table 1
Summary of the CVMix K-Profile Parameterization Default Configuration

Parameterization choice	CVMix default value
OSBL interpolation	Quadratic
Internal matching	Only match to diffusivity and viscosity
Interpolation order for internal matching	Linear
Convective diffusion	Enabled
$\mathrm{Ri}_{\mathrm{crit}}$ (critical Richardson number)	0.25
ϵ (fraction of OBSL occupied by surface layer)	0.1
Enhanced diffusivity at OSBL base	Enabled
Shear instability-driven mixing	LMD94 scheme

Note. CVMix = Community ocean Vertical Mixing project; OSBL = ocean surface boundary layer.

2000; Reichl et al., 2016; Smyth et al., 2002). One excellent example of complex forcing in an ocean LES comparison is that in Large and Gent (1999) wherein large-scale ocean circulation model forcing was incorporated to examine the diurnal variability of the equatorial thermocline. Unlike other previous studies (Bachman et al., 2017; Hamlington et al., 2014; Whitt & Taylor, 2017), here we ignore influences of lateral gradients. We do so to reduce the computational cost of each test case, to minimize the complexity of initial conditions, and to focus on examining the influence of physical assumptions within KPP as well as numerical implementation choices. Our chosen test suite facilitates an examination of KPP under a broader range of controlled forcing scenarios relevant for simulating the ocean climate system.

1.4. Organization of This Paper

We start the main portion of this paper in section 2, where we summarize physical and numerical elements of KPP and present salient implementation considerations and issues. The LES model and test cases are discussed in section 3, and then we describe results and analysis in sections 4–7. The presentation of results focuses on issues discussed in section 2 and offers possible solutions. We close the main portion of the paper with conclusions and recommended best practices in section 8. Various appendices offer further details concerning physical and numerical aspects of KPP and our benchmarking test cases.

2. KPP Considerations

The primary scope of this work is to (1) reexamine and clarify critical aspects of LMD94, for example, matching of KPP to internal mixing parameterizations at the OSBL base, the parameterization of entrainment, and the nonlocal tracer flux parameterization, and (2) introduce and test new configuration options of KPP, for example, the disabling of matching to interior mixing parameterizations (section 2.4), and a reformulation of the V_t^2 parameterization (section 2.5.1). We present here some salient points that elucidate our reexamination and introduces our new configuration options. Additional KPP formulation details are given in Appendix B. A table of mathematical symbols along with preferred units is given in Appendix A.

2.1. Basic Definitions

The vertical position in the ocean, z, ranges from

$$-H(x,y) \le z \le \eta(x,y,t), \tag{1}$$

where $z = -H$ is the position of the static ocean bottom, $z = \eta$ is the position of the dynamic ocean free surface, $z = 0$ is the resting ocean surface (reference geopotential), and

$$\text{depth} = -z + \eta \ge 0 \tag{2}$$

is the positive distance from the ocean surface to a point in the ocean. When referring to positions within the surface boundary layer, it is convenient to use a nondimensional boundary layer coordinate

$$\sigma \equiv \frac{-z+\eta}{h} \qquad 0 \le \sigma \le 1, \tag{3}$$

where $\sigma = 0$ at the ocean free surface and $\sigma = 1$ at the boundary layer base where

$$-z + \eta = h \qquad \text{OSBL thickness.} \tag{4}$$

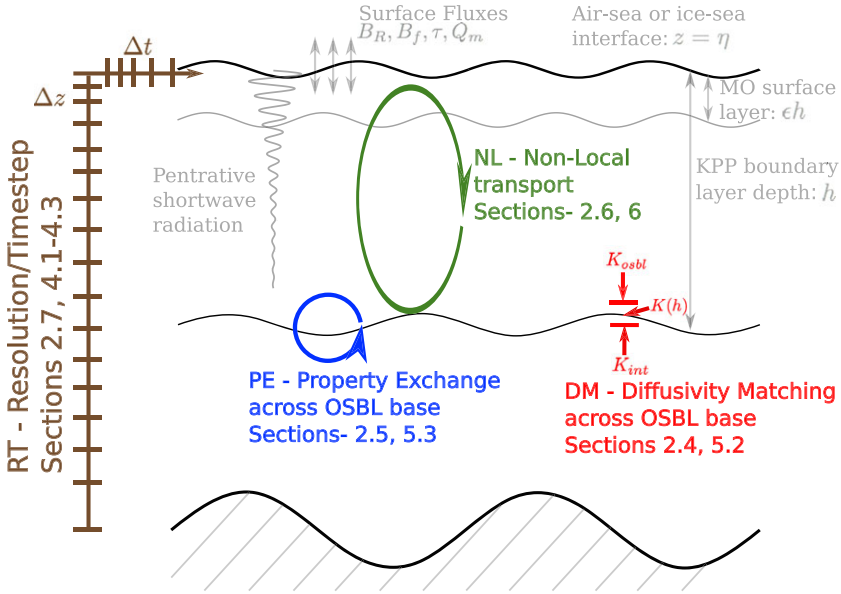

Figure 1. Schematic of the upper ocean regions associated with the KPP boundary layer parameterization. The upper ocean is exposed to fluxes of momentum, τ, mass, Q_m, and buoyancy, B_f, at the air-sea interface. Penetrating shortwave radiation, $(\overline{w'\theta'})_R$, along with its associated buoyancy flux, $B_R > 0$, also influences the upper ocean. The MO surface layer transfers these fluxes to the remainder of the boundary layer. Here we assume the surface layer extends from the free surface ($z = \eta$) to $z = \eta - \epsilon h$, where $h > 0$ is the depth of the boundary layer base (typically $\epsilon \approx 0.1$). The colored portions of the schematic represent the four components of KPP we focus on in this paper (section 2). The red section represents the diffusivity matching (DM) in KPP, where K_{osbl}, K_{int}, and $K(h)$ are the diffusivities at the last layer in the OSBL, the first model layer below the OSBL, and at the OSBL, respectively. The green signifies the nonlocal (NL) parameterization, the blue represents entrainment and detrainment across the OSBL base (i.e., property exchange, PE), and the brown represents the influence of choices in the calling model on KPP fidelity. Here we focus on vertical resolution and model time step (RT). The sections for each color denotes the portions of the paper where that process is examined. KPP = K-profile parameterization; MO = Monin-Obukhov; OSBL = ocean surface boundary layer.

2.2. General Structure of the KPP Parameterization

For any prognostic scalar or vector field component ψ (e.g., tracer concentration and velocity component), the KPP scheme parameterizes the turbulent vertical flux within the surface boundary layer according to

$$\overline{(w'\psi')} = -K_\psi \frac{\partial \psi}{\partial z} + K_\psi \gamma_\psi, \tag{5}$$

where ψ' represents the subgrid scale fluctuation relative to ψ. The first right-hand side term represents the local contribution to the turbulent vertical flux of ψ, and the second term is the parameterized nonlocal flux. The eddy diffusivity K_ψ is written as the product of three terms

$$K_\psi = h\, w_\psi(\sigma) G(\sigma), \tag{6}$$

where h is the KPP diagnosed OSBL depth (equation (4)) and $G(\sigma)$ is the vertical shape function. The CVMix KPP algorithm to determine the boundary layer depth is discussed in section 2.3.

As shown by equation (6), the boundary layer depth $h > 0$ scales the diffusivity, so that K_ψ increases as the boundary layer deepens. Consequently, the behavior of KPP is critically dependent on the boundary layer depth. Furthermore, the vertical structure of the KPP diffusivity, and hence, the nonlocal flux (equation (5)) are set by the nondimensional shape function, $G(\sigma)$.

In this work we focus on four main physical and numerical processes denoted by colors in Figure 1:

- DM: matching the diffusivity and its gradient at the OSBL base (red);
- PE: property exchange (i.e., entrainment and detrainment) across the OSBL base, resulting from diffusivity at the OSBL base (blue);
- NL: nonlocal transport (green);
- RT: model resolution and time step (brown).

All of the processes in Figure 1 are influenced by the KPP-diagnosed OSBL depth, h. Hence, the KPP OSBL depth algorithm is pivotal to the performance of the scheme, with further details of its calculation provided in section 2.3. Our four focus areas are introduced afterward.

2.3. Bulk Richardson Number and the Boundary Layer Depth

The bulk Richardson number in KPP is computed by

$$\mathrm{Ri_b} = \frac{(b_{sl} - b(z))\,(-z + \eta)}{|\mathbf{u}_{sl} - \mathbf{u}(z)|^2 + V_t^2(z)}. \tag{7}$$

The bulk Richardson number relates the gain in potential energy (numerator) of boundary layer filling eddies to the loss of kinetic energy (denominator). In this expression, b is the buoyancy (dimensions of length per squared time) based on the surface referenced potential density and b_{sl} is the buoyancy averaged over the depth of the surface layer between the depth range $0 \le \sigma \le \epsilon$ (see Figure 1). Small differences of $b_{sl} - b(z)$ signal weak vertical stratification, characteristic of a region within the surface boundary layer. In contrast, large differences arise when z reaches into the more stratified region beneath the boundary layer. The denominator in $\mathrm{Ri_b}$ consists of the squared vertical shear resolved by the model's prognostic horizontal velocity field: $|\mathbf{u}_{sl} - \mathbf{u}(z)|^2$, where $\mathbf{u}_{sl}$ is the surface layer averaged horizontal velocity. In addition, the term V_t^2 aims to parameterize unresolved vertical shears near the OSBL base resulting from the turbulent energy of boundary layer eddies near the boundary layer base (see section 2.5.1). When either the resolved or parameterized shear is large (denominator of equation (8)), the bulk Richardson number is reduced and the OSBL deepens. Finally, note that even if the buoyancy difference and vertical shear are vertically constant, the bulk Richardson number increases linearly with depth, $d = -z + \eta$, given the presence of depth in the numerator of equation (7).

In most implementations of KPP (except the Regional Ocean Modeling System implementation [Lemarié et al., 2012] of KPP, which uses an alternative integral formulation), the depth at the base of the ocean surface boundary layer, $-z + \eta = h$, is diagnosed as the depth where the bulk Richardson number first equals a critical value

$$\mathrm{Ri_b} = \mathrm{Ri_{crit}} = \frac{(b_{sl} - b(h))\,h}{|\mathbf{u}_{sl} - \mathbf{u}(h)|^2 + V_t^2(h)}. \tag{8}$$

In LMD94, the critical bulk Richardson number was set to $\mathrm{Ri_{crit}} = 0.3$ and represents an empirical fit to available ocean observations. We note that values between 0.25 and 1.0 have been used in similar formulations (e.g., McGrath-Spangler et al., 2015; Troen & Mahrt, 1986; Vogelzang & Holtslag, 1996). Theoretical values of $\mathrm{Ri_{crit}}$ vary from $\mathrm{Ri_{crit}} = 0.25$ for shear instability when using a linear stability analysis (Miles, 1961). This definition may not be appropriate for weak mean shear and breaking internal waves (Barad & Fringer, 2010; Troy & Koseff, 2005) to O(1) for a nonlinear stability analysis (Abarbanel et al., 1984). However, Troen and Mahrt (1986) argue that shear may not be adequately resolved in a model simulation, prompting use of a larger value of $\mathrm{Ri_{crit}}$ that is a function of vertical grid spacing.

In general, the correct diagnosis of the boundary layer depth is a key part of the KPP scheme, as this depth controls the upper ocean turbulent layer and the strength of mixing within that layer. The diagnosed boundary layer depth also controls the strength of entrainment into the OSBL (see section 2.5.1). We thus expect the chosen definitions of surface layer fraction (ϵ; Figure 1), parameterized turbulent vertical shear, V_t^2, and the critical bulk Richardson number, $\mathrm{Ri_{crit}}$, to influence KPP results.

It is unlikely that the bulk Richardson number computed at a model interface is exactly equal to the chosen critical threshold. Furthermore, the region near the base of the OSBL is highly nonlinear due to the transition from a relatively well mixed region to a region of high stratification and shear. Consequently, the KPP boundary layer depth is sensitive to the interpolation method used to determine where $\mathrm{Ri_b} = \mathrm{Ri_{crit}}$ according to equation (8) (Danabasoglu et al., 2006; Seidel et al., 2010). For the benchmarking of KPP relative to LES conducted in this paper, we use the KPP bulk Richardson number method based on equation (8) to determine the OSBL depth with LES data.

2.4. Shape Function and Diffusivity Matching

The vertical shape function, $G(\sigma)$, controls the vertical structure of diffusivity and the nonlocal flux in KPP (equation (6)). The shape function is assumed to follow a cubic polynomial as proposed by O'Brien (1970). The method to determine the polynomial coefficients is given in Appendix B1 and LMD94. Here we iden-

tify potential issues with the matching of diffusivities from KPP to those determined by interior mixing parameterizations (e.g., the shear instability-induced mixing parameterization of LMD94).

2.4.1. Problems Matching Diffusivity Derivatives at the OSBL Base

The KPP diffusivity matching proposed by LMD94 means that parameterized turbulence generated in the ocean interior (e.g., internal waves and shear instabilities) indirectly influences the diffusivity within the surface boundary layer. In LMD94, interior diffusivity parameterizations assumed a constant value or followed a relatively simple formula. In modern calling models, interior-generated diffusivities can have nontrivial vertical structure (either increasing or decreasing when moving toward the boundary layer base). Hence, the magnitude of the vertical derivative of diffusivity can be large. Consequently, there is no guarantee that the KPP diffusivity will vary smoothly across the OSBL base. Further, the vertical derivative of the diffusivity can be sharp (i.e., discontinuous) near the OSBL base, which leads to a generally poor representation on a discrete vertical grid. Given these potential difficulties, in section 6.2 we test the sensitivity of KPP to three variants of internal matching: matching the internal diffusivity and its gradient, matching the internal diffusivity alone, and abandoning matching altogether.

2.4.2. Problems With the Nonlocal Parameterization at the OSBL Base

With multiple turbulent processes active in and near the surface boundary layer, we are confronted with the question of how these processes interact. Do they add, multiply, or cancel? As proposed by Large et al. (1994), KPP traditionally chooses to match boundary layer diffusivities to those active below the boundary layer. However, in section 6.2 we show that an additive or dominance-based approach can reduce the OSBL bias relative to LES in certain test cases. The full diversity of interactions between the many different classes of turbulence present in the upper ocean is an active area of research outside of our scope.

The KPP nonlocal tracer flux parameterization acts to redistribute the surface tracer flux through the depth of the boundary layer. Thus, we do not expect the nonlocal tracer flux parameterization to be active at and below the OSBL base. Neglecting diffusivity matching allows the nonlocal parameterization to naturally tend to 0 at the OSBL base. In contrast, retaining a nonzero diffusivity at the OSBL base retains a nonzero nonlocal term at the OSBL base. Even if KPP were extended to include interactions with additional processes at the OSBL base (e.g., the turbulent transition layer, entrainment by roll vortices, and intermittent plumes) it is unclear if these interactions would/should modify the KPP nonlocal term.

2.5. Property Exchanges Across the OSBL Base

Property exchanges at the OSBL base are determined in two ways: a parameterization of unresolved turbulence (V_t^2) and the enhanced diffusivity parameterization. The V_t^2 parameterization exerts a strong influence at fine vertical resolution, while the enhanced diffusivity dominates at coarser vertical resolution. We discuss both in this section.

2.5.1. The Parameterization of V_t^2 in $\mathrm{Ri_b}$

The KPP scheme includes a term related to the kinetic energy of unresolved turbulence (V_t^2) in the bulk Richardson number denominator in equation (7). The purpose of this term is to sufficiently deepen the OSBL to ensure that the empirical rule of free convection is satisfied. The entrainment depth is defined as the depth of the minimum turbulent buoyancy flux, where the empirical rule of convection (see LMD94) gives this flux as

$$\overline{(w'b')}_{\mathrm{h_e}} \approx -0.2\,\overline{(w'b')}_{\mathrm{sfc}}, \tag{9}$$

where h_e is the entrainment depth (see Figure 2). In addition to being the depth of the minimum buoyancy flux, the entrainment depth is where water from below the boundary layer is exchanged with boundary layer water.

The parameterization of V_t^2 is derived by considering a buoyancy profile that is well mixed to a given depth (h_{m}) with linear stratification below (Figure 2). The buoyancy flux at h_e is written (using equations (5) and (6)) as

$$\overline{(w'b')}_{\mathrm{h_e}} = -h\,w_b(\sigma)\,G(\sigma)\left(\frac{\partial b}{\partial z} - \gamma_b\right) \qquad \text{with} \quad \sigma = \frac{h_e}{h} \tag{10}$$

where w_b is a turbulent velocity scale (equation (B3)). Near the boundary layer depth, h, the nonlocal term γ_b (see equation (19)) is small and can be ignored. Furthermore, in convective conditions,

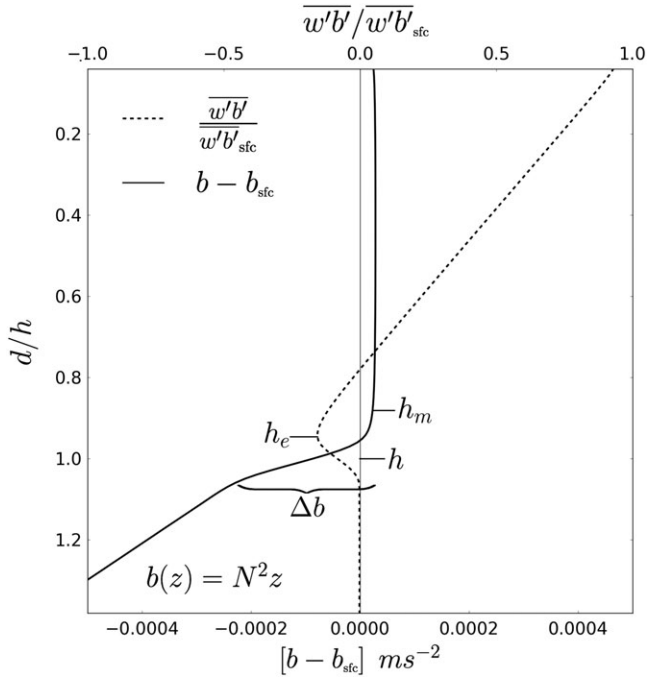

Figure 2. Schematic illustrating the various depths arising in the boundary layer as forced by a destabilizing surface buoyancy flux, in which case $(\overline{w'b'})_{\rm sfc} > 0$ (defined in equation (33)). This forcing supports active nonlocal convective boundary layer turbulence. Data for this figure are taken from the large eddy simulation results of the free convection (FC) experiment (Figure 4a). The vertical axis is the nondimensional depth, $\sigma = (-z + \eta)/h$, extending from beneath the boundary layer base ($\sigma > 1$) to the base of the surface layer ($\sigma = \epsilon$) (see Figure 1). The dashed line is the local turbulent buoyancy flux, $(\overline{w'b'})$, normalized by the surface buoyancy flux $(\overline{w'b'})_{\rm sfc}$. The scale for this ratio is along the top axis. Depths where $(\overline{w'b'})/(\overline{w'b'})_{\rm sfc} < 0$ are where the local turbulence stabilizes the boundary layer, which occurs near the boundary layer base. The solid line is the difference in local buoyancy and the surface layer buoyancy, $b - b_{\rm sfc}$, with corresponding scale along the bottom axis (in units of 10^{-4} m/s^2). The mixed layer is where buoyancy is weakly stratified, $\partial b/\partial z \approx 0$. The mixed layer base is determined subjectively by $\partial b/\partial z > (\partial b/\partial z)_{\rm min} > 0$, with $(\partial b/\partial z)_{\rm min}$ a chosen minimum stratification criteria. For much of the boundary layer, $b - b_{\rm sfc} > 0$, since the surface layer buoyancy is driven low by the destabilizing surface flux. The entrainment depth, h_e, is where $(\overline{w'b'})/(\overline{w'b'})_{\rm sfc} < 0$ reaches a minimum, with h_e straightforward to diagnose in a large eddy simulation. Appendix F discusses an idealized buoyancy profile similar to that shown here that allows for an analytic expression for h. In the entrainment layer, buoyancy changes rapidly (Δb), reflecting enhanced vertical stratification below the boundary layer. Below the entrainment layer, the buoyancy profile is roughly constant ($b \approx N^2 z$ with $N^2 > 0$ constant and $z < 0$). The K-profile parameterization boundary layer depth, h, is determined by the bulk Richardson number criteria in equation (8).

$$w_b(h_e/h) \to \kappa \left(c_s \kappa \epsilon\right)^{1/3} w_* , \tag{11}$$

where κ is the von Kármán constant, c_s is an empirical constant, and w_* is the convective turbulent velocity scale (Deardorff, 1970) defined as

$$w_* \equiv (-h\,(\overline{w'b'})_{\rm sfc})^{1/3}. \tag{12}$$

Also, noting that the $N_e^2 = (\partial b/\partial z)_e$ and $h_e \approx h$, where N_e is the entrainment layer stratification, equation (10) becomes

$$(\overline{w'b'})_{h_e} = -\kappa \left(c_s \kappa \epsilon\right)^{1/3} w_* \left(1 - \frac{h_e}{h}\right)^2 h\, N_e^2 \tag{13a}$$

$$= -\kappa \left(c_s \kappa \epsilon\right)^{1/3} w_* \left(h - h_e\right)^2 N_e^2/h. \tag{13b}$$

At the OSBL base, $\mathrm{Ri_b} = \mathrm{Ri}_{\rm crit}$ (see equation (8)), which can be used to write an expression for V_t^2. By assuming the resolved vertical shear is 0 we have

$$\mathrm{Ri}_{\mathrm{crit}} = \frac{h\,(b_{\mathrm{sl}} - b(h))}{V_t^2}. \tag{14}$$

Given the assumed linear buoyancy profile, the numerator of equation (14) is $h\,N_e^2(h - h_e)$, which implies

$$h - h_e = \frac{V_t^2\,\mathrm{Ri}_{\mathrm{crit}}}{h\,N_e^2}. \tag{15}$$

Using equations (14) and (15) brings equation (13b) into the form

$$\overline{(w'\,b')}_{\mathrm{h_e}} = -\kappa\left(c_s\kappa\epsilon\right)^{1/3} w_*\,V_t^4\,\mathrm{Ri}_{\mathrm{crit}}^2\,N_e^2/(N_e^4\,h^3). \tag{16}$$

If the empirical rule of convection (equation (9)) is enforced in equation (16), then we can solve for V_t^2 so that

$$V_t^2 = \frac{\sqrt{0.2}\,C_v}{\mathrm{Ri}_{\mathrm{crit}}\,\kappa^{2/3}}\left(c_s\,\epsilon\right)^{-1/6} h\,N_e\,w_*. \tag{17}$$

In LMD94, ocean observations were used to determine a constant C_v such that the model diagnosed N_e is equivalent to $C_v \times N_e(h_e)$, where $N_{obs}(h_e)$ is the observed entrainment layer stratification.

Note that N_e is the stratification within the entraining layer. This approach contrasts to the use of stratification below the OSBL suggested by Danabasoglu et al. (2006; their Appendix A). Both options are tested relative to LES in sections 6.1.1.

2.5.2. The LMD94 Enhanced Diffusivity Parameterization

For coarse vertical resolution, LMD94 propose the addition of an enhanced diffusivity to partially mitigate resolution-dependent biases. Here we suggest that the enhanced diffusivity parameterization also serves to parameterize unresolved sources of entrainment.

In their Appendix D, LMD94 note that as vertical resolution coarsens near the OSBL base, *staircase* structures can emerge in the time series of the boundary layer depth. We show this behavior in Figure 4a discussed in section 4. To understand the cause of the staircase structures, start by assuming the OSBL base is aligned with a grid cell center. Furthermore, as in the case discussed in LMD94 (and the free convection test case described in section 3.2), assume zero vertical property gradients within the boundary layer. Now allow the OSBL to deepen further into the grid cell. As it deepens, boundary layer-induced mixing at the next grid interface below is not possible until the boundary layer reaches the bottom of this cell. Once the OSBL depth deepens into the next model cell, diffusivities jump to a larger value, in which case properties mix quickly. The resulting time series of boundary layer properties thus exhibits a stair-step structure.

Use of a quadratic interpolation scheme, where the stencil for quadratic interpolation includes the first model level where $\mathrm{Ri}_b > \mathrm{Ri}_{\mathrm{crit}}$, as well as the two model levels above that layer, to determine the OSBL depth has reduced these staircase structures (Danabasoglu et al., 2006). Nonetheless, we still see such structures in our simulations (e.g., Figure 4a). Fundamentally, the staircase structures in OSBL depth illustrate a lack of an appropriate representation of unresolved entrainment fluxes. The V_t^2 parameterization attempts to represent boundary layer entrainment, but given the dependence of V_t^2 on the modeled stratification near the OSBL base (see equation (17)), entrainment in KPP will be strongly resolution dependent. The LMD94 enhanced diffusivity parameterization also acts to enhance entrainment fluxes (section 6.3) by increasing the KPP predicted diffusivity near the OSBL base, thus smoothing vertical movement of the boundary layer between grid cells. LMD94 defines the enhanced diffusivity (Λ) at the OSBL base via

$$\begin{aligned} K^*(d_{\mathrm{osbl}}) &= (1-\delta)^2 K(d_{\mathrm{osbl}-1}) + \delta^2 K(d_{\mathrm{osbl}-1/2}), \\ \Lambda(d_{\mathrm{osbl}}) &= (1-\delta)\nu(d_{\mathrm{osbl}-1/2}) + \delta K^*(d_{\mathrm{osbl}}). \end{aligned} \tag{18}$$

Here $d_{\mathrm{osbl}-1}$ is the depth of the first model grid center above the OSBL base, $d_{\mathrm{osbl}-1/2}$ is the depth of the first model interface above the OSBL, δ is the fractional distance between $d_{\mathrm{osbl}-1}$ and the OSBL base, K is the KPP boundary layer diffusivity, and ν is the diffusivity predicted by internal mixing parameterizations. Note that even if $\nu(d_{\mathrm{osbl}-1/2})$ is 0, equation (18) shows that the diffusivity can still be enhanced at the OSBL base given the dependence on K. For additional details on the enhanced diffusivity parameterization, see Appendix D of LMD94.

2.6. The KPP-Parameterized Nonlocal Tracer Transport

The parameterized nonlocal tracer flux from KPP is the product of the diffusivity (equation (6)) and a parameterized nonlocal term. The nonlocal term is nonzero only for tracers (though see Smyth et al., 2002, and Sinha et al., 2015, who suggest forms for nonlocal momentum fluxes, where the latter includes effects from coastal Langmuir turbulence) only in unstable surface buoyancy forcing. It takes the form (e.g., Mailhot & Benoit, 1982), LMD94

$$\gamma_\psi = C_* \kappa \left(c_s \kappa \epsilon\right)^{1/3} \left(\frac{\overline{(w'\psi')}_{\text{sfc}}}{w_\psi h} \right), \tag{19}$$

where κ is the von Kármán constant and c_s and C_* are constants (see LMD94 or Griffies et al., 2015, for details of these constants). The turbulent tracer flux $\overline{(w'\psi')}_{\text{sfc}}$ arises from surface tracer transport due to air-sea or ice-sea interactions (see Appendix C). For potential temperature, the nonlocal flux ($\psi = \theta$) is

$$K_\theta \gamma_\theta \equiv \overline{(w'\theta')}_{\text{nonlocal}} = C_* \kappa \left(c_s \kappa \epsilon\right)^{1/3} G(\sigma) \overline{(w'\theta')}_{\text{sfc}}. \tag{20}$$

Hence, the parameterized nonlocal tracer flux is proportional to the shape function times the surface turbulent tracer flux. Specifically, this form for the KPP nonlocal potential temperature flux identifies it as a vertical redistribution of the surface flux $\overline{(w'\theta')}_{\text{sfc}}$ throughout the boundary layer. The KPP nonlocal fluxes for other tracers take on the same form but with potentially different constants. This form provides a useful conceptual framework for understanding the KPP nonlocal parameterization as well as a guide toward its numerical implementation.

The nonlocal potential temperature flux includes a contribution from penetrating shortwave radiation. However, it is unclear how much of the shortwave absorbed in the boundary layer to include in $\overline{(w'\theta')}_{\text{sfc}}$. Here we follow LMD94 and carry the shortwave radiation absorbed in the OSBL in the nonlocal heat flux parameterization and have found little sensitivity to this choice in our test cases. However, sensitivity to this choice is further discussed in Appendix C1.3.

2.6.1. The Nonlocal Term and Turbulence Closure Theory

The KPP diagnosed turbulent buoyancy flux (equation (5)) consists of two components: a local term proportional to the vertical gradient of buoyancy and a nonlocal term that is independent of the vertical buoyancy gradient. The parameterized nonlocal turbulent buoyancy flux is derived from the turbulent buoyancy flux budget (Note that some atmospheric derivations [e.g., Deardorff, 1972] use the temperature variance equation instead of the turbulent buoyancy flux equation. Yet the form of the resulting parameterization is identical). For atmospheric modeling applications (Deardorff, 1966, 1972; Ertel, 1942; Holtslag & Moeng, 1991; Mailhot & Benoit, 1982), the buoyancy depends solely on virtual potential temperature (e.g., Stull, 2012), and thus, the nonlocal turbulent buoyancy flux directly corresponds to the nonlocal turbulent heat flux. For oceanic applications KPP introduces separate nonlocal flux parameterizations for potential temperature and salinity. To derive these separate parameterizations we first build the turbulent temperature and salinity flux budgets from the w', θ', and S' budgets by invoking nonhydrostatic dynamics, given the general presence of strong vertical motions in the turbulent boundary layer and assuming an f plane. Using these assumptions we have

$$\frac{\partial \overline{w'\theta'}}{\partial t} = \underbrace{-\overline{w'^2}\frac{\partial \bar{\theta}}{\partial z}}_{\text{local}} + \underbrace{g\left(\alpha_\theta \overline{\theta'^2} - \beta_S \overline{\theta' S'}\right)}_{\text{buoyancy production}} - \underbrace{\frac{\partial \overline{w'w'\theta'}}{\partial z}}_{\text{triple moment}} - \underbrace{\overline{\frac{\theta'}{\rho_o}\frac{\partial p'}{\partial z}}}_{\substack{\text{pressure-temperature} \\ \text{covariance}}}, \tag{21}$$

$$\frac{\partial \overline{w'S'}}{\partial t} = \underbrace{-\overline{w'^2}\frac{\partial \bar{S}}{\partial z}}_{\text{local}} + \underbrace{g\left(\alpha_\theta \overline{\theta' S'} - \beta_S \overline{S'^2}\right)}_{\text{buoyancy production}} - \underbrace{\frac{\partial \overline{w'w'S'}}{\partial z}}_{\text{triple moment}} - \underbrace{\overline{\frac{S'}{\rho_o}\frac{\partial p'}{\partial z}}}_{\substack{\text{pressure-salinity} \\ \text{covariance}}}. \tag{22}$$

From the discussion of boundary conditions in Appendix C3, and assuming a linear equation of state, we write the turbulent buoyancy flux as

$$\overline{w'b'} = g\,\overline{w'\,(\alpha_\theta\,\theta' - \beta_S\,S')}, \tag{23}$$

where we assume the thermal expansion and haline contraction coefficients are locally constant so they do not contribute to turbulent fluctuations. Similarly, the buoyancy variance can be written as

$$\overline{b'^2} = g^2\,\overline{(\alpha_\theta\theta' - \beta_S S')^2}. \tag{24}$$

Using equations (23) and (24) we can derive a budget equation for the turbulent buoyancy flux through multiplying equation (21) by $g\,\alpha_\theta$, equation (22) by $g\,\beta_S$, and then taking the difference, namely,

$$\frac{\partial\overline{w'b'}}{\partial t} = -\overline{w'^2}\,\frac{\partial\bar{b}}{\partial z} + \overline{b'^2} - \frac{\partial\overline{w'w'b'}}{\partial z} - \overline{\frac{b'}{\rho_o}\frac{\partial p'}{\partial z}}. \tag{25}$$

Terms on the right-hand side of equation (25) that do not include the vertical gradient of the mean buoyancy correspond to the nonlocal terms in KPP. As seen in the following, the KPP nonlocal tracer transport parameterization derives from the buoyancy variance.

Use of surface similarity theory and a pressure-buoyancy covariance parameterization (e.g., Canuto et al., 2001; Moeng & Wyngaard, 1986) yields

$$\overline{w'b'} \approx -\tau\overline{w'^2}\left(\frac{\partial\bar{b}}{\partial z} + C\frac{\overline{(w'b')}_{\text{sfc}}}{w_* h}\right), \tag{26}$$

where $w_* = [\overline{(w'b')}_{\text{sfc}}h]^{1/3}$ is the convective velocity scale (section 2.5.1) and C is a constant. The first term on the right-hand side of equation (26) is parameterized by KPP using a flux gradient expression, whereas the second is parameterized by a nonlocal redistribution of the surface turbulent buoyancy flux throughout the boundary layer. KPP includes surface momentum forcing effects in equation (26) by replacing w_* with w_s (equation (B3)), given that w_s is dependent on u_*.

To split the nonlocal buoyancy flux parameterization (equation (26)) into separate parameterizations for a nonlocal heat and salt flux (see equation (19)) we assume that the thermal and haline expansion coefficients are constant throughout the OSBL and within the calling model grid cell. We make this assumption even though these values may change over larger length and timescales within the calling model. As a result, KPP can compute a nonlocal transport when there is a destabilizing surface flux of either heat or salt. We examine the KPP nonlocal transport term relative to LES in section 7.

2.6.2. Parameterized Nonlocal Salt Transport

LMD94 formulated KPP for models with a virtual salt flux at the ocean surface. For a virtual salt flux, the nonlocal salt fluxes are directly implemented just as the nonlocal heat fluxes given by equation (20). However, in models making use of a freshwater surface boundary condition rather than a virtual salt flux, for example, MPAS-O and MOM6, the salinity in the top layer is changed via surface mass fluxes (arising from precipitation, evaporation, runoff, ice melt/formation, and brine release). Implementation of the nonlocal transport for real water flux models requires a separately defined salt flux given by

$$Q_s = Q_{\text{m}}\,S_{\text{sfc}}, \tag{27}$$

where S_{sfc} is the salinity in the surface grid cell and Q_{m} is the freshwater flux. Equation (27) also applies to all tracers that, like salt, have a high solubility in water and that do not leave the ocean with evaporating water. See Appendix C for more details about surface boundary fluxes.

2.7. Choices Made in the Calling Model

During the development of CVMix, we discovered that certain choices made in the circulation model implementation can influence the results of the one-dimensional KPP tests. For example, as discussed in section 2.5, the KPP V_t^2 parameterization is dependent on stratification near the OSBL; thus, we expect the effectiveness of this parameterization to be sensitive to the chosen model resolution. In our comparisons, we test a variety of vertical grid spacings (0.1 to 10 m). Comparisons to LES confirm that there is indeed a resolution-dependent bias. We discuss this bias and possible remedies in section 4.1.

MPAS-O, POP, and MOM6 utilize different time stepping schemes. We thus do not presume, before testing, that results are robust across the models. Despite the different time stepping schemes, each model computes the vertical mixing tendency implicitly in time to avoid numerical stability restrictions on the time step. However, due to sensitivity to the parabolic Courant number (Lemarié et al., 2015) there can be biases that grow with the time step (Lemarié et al., 2012). In section 4.2 we test the sensitivity of KPP to the chosen time step following the test case in Reffray et al. (2015).

In all models the interior shear-driven mixing parameterization of LMD94 is used when surface momentum forcing is imposed. The diffusivity and viscosity resulting from shear instability are assumed to be given by a polynomial function of the gradient Richardson number (see equation (28) in LMD94).

3. The LES Model and the One-Dimensional Test Cases

We here present the LES model used for establishing a baseline behavior to be compared with KPP and then summarize the one-dimensional oceanic test cases used to benchmark KPP.

3.1. LES Model

We compare one-dimensional column tests of KPP to a mature and commonly utilized LES model (Moeng & Wyngaard, 1984; McWilliams et al., 1997; Sullivan et al., 2007). The LES utilizes the Deardorff (1980) subgrid parameterization with the stability functions of LMD94 to parameterize the surface layer. The LES model also uses the third-order Runge-Kutta time stepping scheme and is pseudo-spectral.

The LES results provide a target for the KPP simulations and thus provide a useful point of comparison. We have made two key modifications to the LES code for our tests. First, we include salinity by setting the buoyancy equal to

$$b = -g\left[1 - \alpha_\theta\left(\theta - \bar{\theta}\right) + \beta_S\left(S - \bar{S}\right)\right]. \tag{28}$$

In this equation, $\alpha_\theta > 0$ is the thermal expansion coefficient, $\beta_S > 0$ is the haline contraction coefficient, and the overline represents a horizontal average over the domain. We choose the constant values

$$\alpha_\theta = 2 \times 10^{-4}\mathrm{K}^{-1}, \tag{29a}$$

$$\bar{\theta} = 298.15\mathrm{K}, \tag{29b}$$

$$\beta_S = 8 \times 10^{-4}\mathrm{ppt}^{-1}, \tag{29c}$$

$$\bar{S} = 35\mathrm{ppt}. \tag{29d}$$

In addition, the buoyancy production terms in the subgrid TKE scheme have been modified so that equation (23) is satisfied. Next, the stability factor in the length scale parameterization (Deardorff, 1980) has been modified, with evaluation of these changes presented in Appendix D.

An additional modification involves the implementation of a diurnal cycle in the LES model along with shortwave radiation (similar to Wang et al., 1998). The vertical penetration of incoming solar radiation follows a two-band exponential formulation with constant extinction coefficients of a Jerlov type IB water mass (Paulson & Simpson, 1977), which is consistent with that used in MPAS, POP, and MOM6 KPP tests. The function describing the time variation of surface shortwave radiation is described in Appendix E.

3.1.1. Details of the LES Test Cases

In most simulations, the LES utilizes a stretched grid over its 150-m vertical extent, with the first layer thickness of 0.1 m. The LES has a horizontal extent of 128 m and a uniform horizontal resolution of 0.5 m. For the surface heating and wind forced case, the LES resolution is uniform in the horizontal and vertical at 0.25 m. In every simulation we have also tested the sensitivity of the LES to horizontal and vertical resolution by doubling the resolution for a short test run. The sensitivity tests yielded little change in the horizontally averaged statistics; thus, we conclude our test cases are not sensitive to the chosen resolution. We have also verified that our

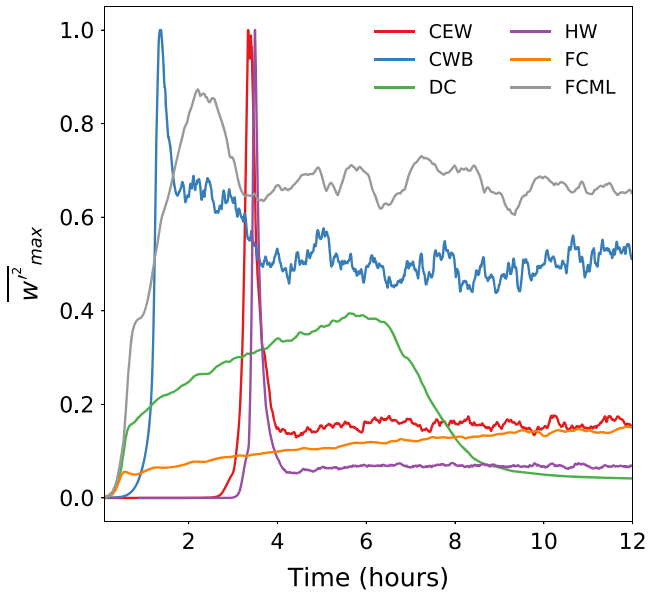

Figure 3. Time variation of the maximum vertical velocity variance ($\overline{w'^2}$) in depth normalized by the maximum vertical velocity variance in time for each simulation. Each colored line corresponds to a large eddy simulation test case. Each line includes the sum of the large eddy simulation resolved and subgrid scale contributions. CEW = cooling, evaporation, and wind; CWB = cooling with background shear; DC = diurnal cycle; HW = heating and wind; FC = free convection; FCML = free convection with a mixed layer.

results are not sensitive to the horizontal domain width by showing that LES model variables decorrelate over the length of the of the horizontal domain (not shown).

All LES cases experience a transition to turbulence, wherein the turbulence kinetic energy increases rapidly and then equilibrates. The transition to turbulence is illustrated in Figure 3, as the rapid increase in the normalized, maximum $\overline{w'^2}$ in depth. KPP is not expected to simulate this transition, and thus, we cannot compare LES to KPP simulations before turbulence is well developed in the LES. In our test cases, small-amplitude noise is seeded in the top six layers to quicken the transition to turbulence and allow for a longer record of LES comparison with KPP. The noise is constructed to ensure that no horizontal mean vertical velocities are created.

We note a few limitations of our LES cases. First, we do not consider the influence of potentially important processes such as Langmuir turbulence, breaking waves, and bubbles. The latter two are not represented by KPP, and the Langmuir turbulence has only recently been implemented, and thus, the Langmuir turbulence modifications will be examined in our future work. Second, we only have one ground truth for each forcing scenario. Hence, results may not be generalizable to all strengths of imposed surface forcing.

3.2. Description of the Test Cases

We examine the impacts of the KPP considerations discussed in sections 2.4–2.7 through a series of one-dimensional test cases. These tests span a range of oceanographically relevant forcing and include the following.

- FC (free convection): convective deepening induced by surface cooling with no initial OSBL (linearly stratified in temperature),
- WNF (wind without Coriolis): OSBL deepening dominated by wind stress with no initial OSBL,
- HW (heating and wind): OSBL deepening via wind stress with surface heating,
- CEW (convection evaporation wind): OSBL deepening generated by mechanical and thermodynamic forcing with no initial OSBL,
- FCML (free convection with a mixed layer): turbulence generated by surface cooling with a preexisting thermocline and halocline,
- CWB (convection wind and background shear): the influence of boundary layer deepening into preexisting background shear,
- DC (diurnal cycle): the influence of diurnal variability in surface buoyancy forcing.

For identification purposes, the tests are named according to their salient details. For example, the test forced by surface cooling, evaporation, and wind is designated CEW. We show the names and key details in Table 2, whereas more complete details are given in Tables 3 and 4.

Table 2
Test Case Names and Salient Features

Test name	Salient details
FC	Free convection
CEW	Surface cooling, evaporation, and wind stress
FCML	Free convection with *T* & *S* mixed layers
WNF	Wind stress with no Coriolis
CWB	Surface cooling and wind stress with background shear
FCE	Free convection due to surface evaporation
DC	Diurnal cycle
HW	Surface heating and wind stress

Table 3
Summary of Forcing Scenarios Considered in the Test Cases

	Q_o (W/m^2)	Q_{sw}^{max} (W/m^2)	E (mm/day)	τ_x (Pa)	$T(z), S(z)$	f (s^{-1})
FC	−75	0	0	0	A	10^{-4}
CEW	−75	0	1.37	0.1	A	10^{-4}
FCML	−75	0	0	0	C	10^{-4}
WNF	0	0	0	0.1	D	0
CWB	−75	0	0	0.1	E	0
FCE	0	0	1.37	0	B	10^{-4}
DC	−75	235.62	0	0	A	10^{-4}
HW	75	0	0	0.1	A	10^{-4}

Note. Q_o is the nonsolar surface heat flux (positive is into the ocean), and Q_{sw}^{max} is the maximum of surface diurnal shortwave radiation. We provide details of the diurnal shortwave forcing in Appendix E. E is the surface evaporation rate, τ_x is the zonal wind stress, and $\tau_y = 0$ in all simulations. $T(z)$ and $S(z)$ are respectively the initial temperature and salinity profiles, which are given in Table 4. The Coriolis parameter (f) is held fixed for a given simulation. In CWB, a background shear is imposed (equation (30)). The FCE test is used to verify the LES implementation of salinity in Appendix D. CEW = cooling, evaporation, and wind; CWB = cooling with background shear; DC = diurnal cycle; FC = free convection; FCE = free convection due to surface evaporation; FCML = free convection with a mixed layer; HW = heating and wind; WNF = wind without Coriolis.

In nearly all test cases, only surface forcing is considered. However, in CWB, a constant background shear layer is imposed via a background velocity profile given as

$$\bar{U}(z) = \begin{cases} 0, & \text{if } z > -25, \\ -\frac{0.3}{50.0}(z+25), & \text{if } z \le -25 \text{ and } z > -75, \\ 0, & \text{otherwise.} \end{cases} \tag{30}$$

Here the imposed shear is roughly equivalent to observed shear in the equatorial undercurrent (Johnson et al., 2002). This shear is imposed as an external forcing in the LES and MPAS-O. For the CWB case, the LES momentum and buoyancy equations become

$$\frac{\partial \mathbf{u}}{\partial t} + (\boldsymbol{\omega} + \mathbf{f}) \times (\mathbf{u} + \bar{U}(z)) = -\nabla \left(p + \frac{1}{2} |\mathbf{u} + \bar{U}(z)|^2 \right) + b\,\mathbf{z} \tag{31a}$$

$$\frac{\partial b}{\partial t} + (\boldsymbol{u} + \bar{U}(z)) \cdot \nabla b = 0. \tag{31b}$$

The inclusion of $\bar{U}(z)$ in the LES is accomplished by adding equation (30) to the LES-resolved zonal momentum prior to computing right-hand side accelerations and then removing this profile prior to updating

Table 4
Initial Temperature (°C) and Salinity (ppt) Profiles Used in the Experiments Given in Table 3

Profile	$T(z)$	$S(z)$
A	$20 + 0.01z$	35
B	20	$35 - 0.007813z$
C	$\begin{cases} 20 & z > -25 \\ 20 + 0.01(z+25) & z \le -25 \end{cases}$	$\begin{cases} 35 & z > -25 \\ 35 - 0.03(z+25) & -35 < z \le -25 \\ 35.3 & z \le -35 \end{cases}$
D	$20 + 0.05z$	35
E	$\begin{cases} 20 & z > -25 \\ 20 + 0.05(z+25) & z \le -25 \end{cases}$	35

Note. Recall that the vertical position (geopotential coordinate z) is positive upward, with $z = 0$ at the resting ocean surface and $z < 0$ in the ocean interior.

Table 5
List of Theory and Results Sections Associated With the Implementation Considerations Shown in Figure 1

Experiment	Description	Results	Relevant tests
Diffusivity matching	2.4	6.2	CEW, FCML
Property exchange	2.5	6.3	FC, CEW, FCML, WNF, DC
Nonlocal transport	2.6	7	CEW, FCML, CWB
Resolution and time step	2.7	4	FC, CEW, WNF

Note. The final column lists each test case pertinent to each individual issue. CEW = cooling, evaporation, and wind; CWB = cooling with background shear; DC = diurnal cycle; FC = free convection; FCML = free convection with a mixed layer; WNF = wind without Coriolis.

the LES-resolved zonal momentum. This choice also ensures that the subgrid parameterization *feels* the background shear as well.

The reduced momentum equation for the KPP tests is

$$\frac{\partial \mathbf{u}}{\partial t} \approx \frac{\partial}{\partial z}\left(\kappa \frac{\partial(\mathbf{u}+\bar{U})}{\partial z}\right). \tag{32}$$

In MPAS-O we simply add equation (30) to the tridiagonal solve routine. We also include this external forcing in the call to the LMD94 shear-driven mixing parameterization and the boundary layer depth computation routine (i.e., it is added in the denominator of equation (8)). The implementation we have chosen here allows for a direct comparison between the LES and KPP.

A number of specifications common to most test cases are the following:

- Equation of state and buoyancy forcing: We use a linear equation of state (equation (28)). The values of α_θ and β_S used in equation (28) are identical to those used for the LES (see equations (29) and (29)). Given a linear equation of state, the surface buoyancy flux is given by

$$\overline{w'b'}_{\text{sfc}} = g\left(\alpha_\theta \overline{w'\theta'}_{\text{sfc}} - \beta_S \overline{w'S'}_{\text{sfc}}\right). \tag{33}$$

  Hence, a positive correlation between vertical velocity fluctuations and temperature fluctuations contribute to a positive turbulent buoyancy flux, as does a negative correlation between vertical velocity and salinity fluctuations.
- Simulation length: Most simulations are run for eight days. However, WNF is run for only one day, CWB is run for 4 days, HW is run for 3 days, and FCML is run for 12 days.
- Time step: In most KPP simulations, except those examining time step sensitivity, use a 20-min time step.
- Shortwave in the DC test: In the DC test, the time-dependent shortwave heat flux is constructed such that the daily integrated positive (stabilizing) buoyancy input is balanced by the daily integrated upward (destabilizing) buoyancy flux. The explicit form of the shortwave radiation used in the DC test given in equation (E3) (see Appendix E), and the maximum daily shortwave radiation is listed in Table 3.
- Internal mixing: In all KPP simulations, constant background mixing is disabled. For the FC, FCML, and DC tests (see Table 2) all internal mixing schemes (mixing below the boundary layer) are disabled. Hence, the diffusivity vanishes beneath the boundary layer so that details of diffusivity matching are irrelevant.
- Across all configurations and parameter settings six LES cases were run with more than 100 KPP tests. We present a subset of these tests, emphasizing lessons learned that lead to best practice recommendations.

Finally, we note that most of the test cases outlined here expose more than one physical and/or numerical consideration raised in section 2. Table 5 lists the four focus areas illustrated in Figure 1 as well as the tests pertinent to each consideration. In Table 6, we summarize the labels used for each sensitivity test and changes made to KPP relative to the baseline configuration of Table 1.

4. Analysis of the CVMix Default Configuration

The default configuration of CVMix (Table 1) is compared across MPAS-O, MOM6, and POP to LES in Figure 4 for the free convection (FC), CEW (cooling, evaporation, and wind), diurnal cycle (DC), and HW (heating and

Table 6
Sensitivity Tests Conducted Within Many of the Test Cases Detailed in Tables 3 and 4

Test label	Parameter(s) changed
Base	Follows Table 1
NM	Internal matching disabled
NM_Add	As in test NM, but with interior diffusivity added in the OSBL
NM_noE	Internal matching and LMD94 enhanced diffusivity disabled
N2	$N = \max(N(k_{\text{osbl}} - 1), N(k_{\text{osbl}}))$ as in equation (39)
MB	Match $\partial_z K_\psi^{\text{int}}(h)$ in internal matching

Note. Test labels correspond to figures in sections 4–7. NM = no match.

wind) tests. We also show an analytic solution (see equation (F11) for the FC case, which is derived in Appendix F). Only MPAS-O has been used for the FCML (free convection with a mixed layer) and CWB (cooling with background shear) tests. The three calling models yield very similar OSBL depths, yet they systematically deviate from the LES solution in the FC, HW, and CEW tests. The largest difference between the models is in the DC test for shallow boundary layers in stable forcing, which is due to the assumed minimum boundary layer depth. In POP the minimum OSBL depth is half of the first model thickness whereas MPAS and MOM6 choose the full layer thickness.

At the fine resolutions ($dz = 1$ m), high-frequency temporal OSBL noise develops near the surface during stabilizing buoyancy forcing (e.g., Figure 4c) in the DC test case. This behavior is similar to what is seen in the FC test (Figure 4a, near the start of the simulation). In section 6.3, we further examine these biases and present a possible solution.

Given that MPAS-O, MOM6, and POP are consistent across tests that span important forcing regimes (convective, shear driven, and stable heating) and KPP configurations, we focus on results from MPAS-O for various sensitivity tests in subsequent sections.

4.1. Exhibiting Sensitivity to Vertical Grid Resolution

A number of the test cases (e.g., FC, FCML, and DC) show that, surprisingly, the KPP boundary layer depth is more consistent with LES at coarser grid resolution, with finer grid resolution showing a persistent shallow boundary layer bias. As an example, Figures 4a and 4c illustrate a persistent shallow bias in OSBL depths at fine resolution relative to LES and coarse-resolution KPP results.

To further quantify the resolution-dependent bias, we have examined a range of vertical spacings (0.1 to 20 m) across our six test cases. For each test, we compute the relative OSBL error as

$$RE_{\text{test}}(t) = \frac{OSBL_{\text{test}}(t) - OSBL_{\text{LES}}(t)}{OSBL_{\text{LES}}(t)}, \tag{34}$$

where the subscript *test* indicates a KPP simulation (e.g., $dz = 1$ m). We have plotted the average relative error for the last day of each test case and every vertical spacing in Figure 5. Across all test cases, KPP exhibits sensitivity to the chosen vertical resolution. Consistent with Figure 4, the highest vertical resolution exhibits the most bias in nearly every test case. The resolution that exhibits the least bias also varies across test cases.

4.2. Sensitivity to Time Step

The WNF (wind stress with no Coriolis force) test has been used previously as a benchmark for one-dimensional turbulence models (e.g., Burchard & Bolding, 2001). It is motivated by the laboratory experiment conducted by Kato and Phillips (1969), who measured the deepening of the surface boundary layer in an initial linearly stratified fluid ($N^2 = 10^{-4}\text{s}^{-2}$) forced by a constant surface friction velocity ($u_* = 0.01$ m/s).

The boundary layer depth in the experiment is defined as the depth of the maximum N^2 in the water column, which we refer to as the Kato-Phillips (KP) boundary layer depth (h_{KP}). Kato and Phillips (1969) found that the KP boundary layer depth followed an empirical relation given by

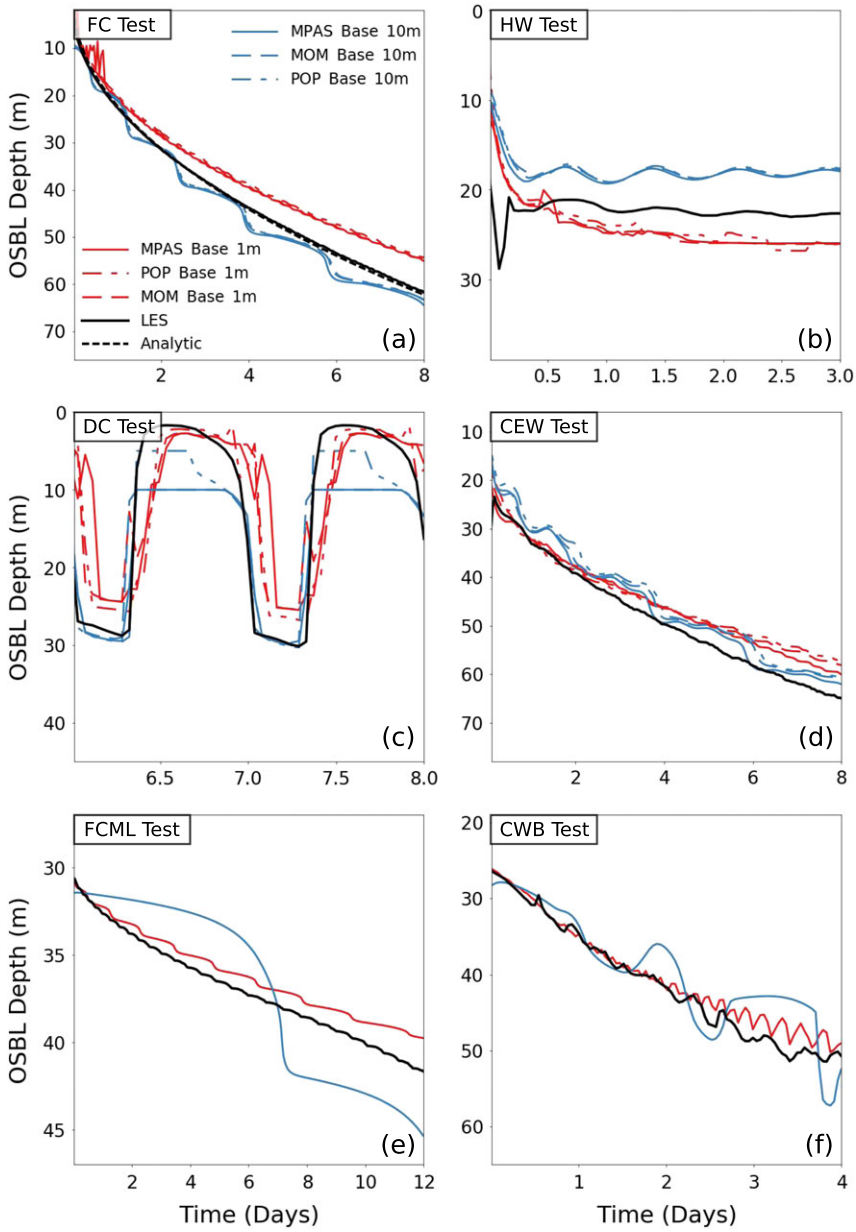

Figure 4. Boundary layer depths diagnosed using equation (8) from the base configuration of MPAS-O, MOM, and POP. (a) Free convection (FC) test, (b) convection, evaporation, and wind (CEW) test, (c) diurnal cycle (DC) test, and (d) heating and wind (HW) test. Results from MPAS-O is also shown for the (e) free convection with a mixed layer (FCML) test and the (f) convection with background shear (CWB) test. The LES output is dashed black. In panel (a), the thick black line is an analytic solution computed from equation (F11). LES = large eddy simulation; MPAS-O = Model for Prediction Across Scales—Ocean; OSBL = ocean surface boundary layer; MOM = Modular Ocean Model; POP = Parallel Ocean Program.

$$h_{KP} = \frac{1.05\, u_* \sqrt{t}}{\sqrt{N(t=0)}}. \tag{35}$$

The WNF test is run for 24 hr as Kato and Phillips (1969) found this relation to hold only for timescales on the order of 30 hr.

Figure 6 shows the root mean square (RMS) relative error averaged over the last 12 hr for the WNF case. Equation (35) is used as the baseline in place of LES results. Our chosen algorithm to diagnose h_{KP} simply locates the level of maximum stratification without interpolation between levels, which could yield oscilla-

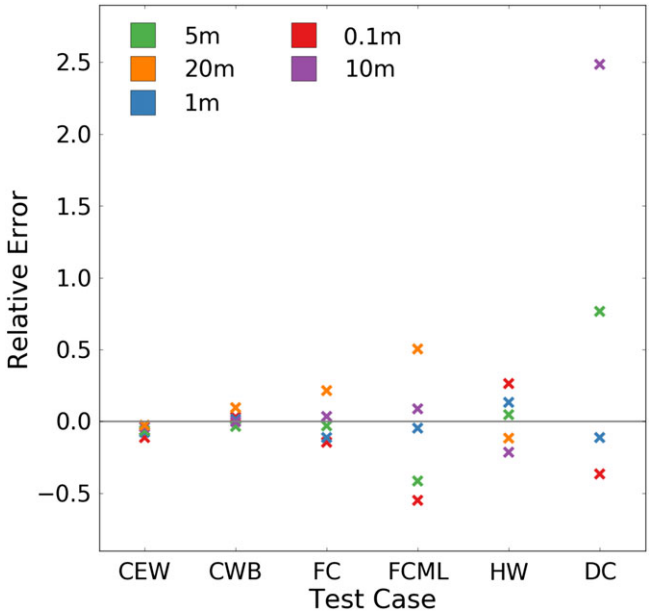

Figure 5. Relative error (equation (34)) averaged over the final day of each test case (Tables 2, 3) for five different vertical grid spacings. The colored markers represent the resolution. For test case DC, the 20-m error is above the *y* axis limit (6.82). CEW = cooling, evaporation, and wind; CWB = cooling with background shear; DC = diurnal cycle; FC = free convection; FCML = free convection with a mixed layer; HW = heating and wind.

tions in the relative error about 0. When time averaged the KPP bias could appear artificially low. Thus, we plot the RMS of equation (34) in Figure 6.

At fine resolution and across all time steps, KPP (in both configurations) captures well the empirical relation given in equation (35), as shown by a small RMS relative error. Coarse-resolution simulations also perform reasonably well across all time steps.

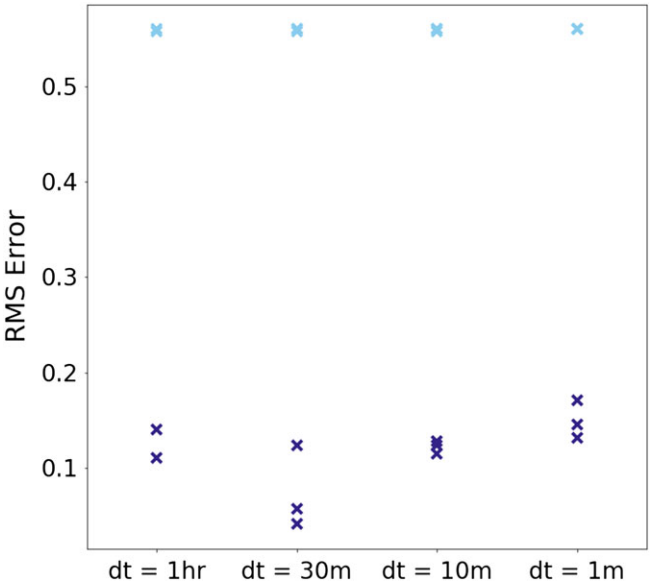

Figure 6. RMS relative error, where equation (35) is used as the reference solution in place of large eddy simulation, from the wind without Coriolis test demonstrating the sensitivity to a chosen time step in K-profile parameterization. The RMS relative error has been averaged over the final 12 hr of the simulation. The cyan markers are for d*z* = 10 m and the purple markers are d*z* = 1 m. RMS = root mean square.

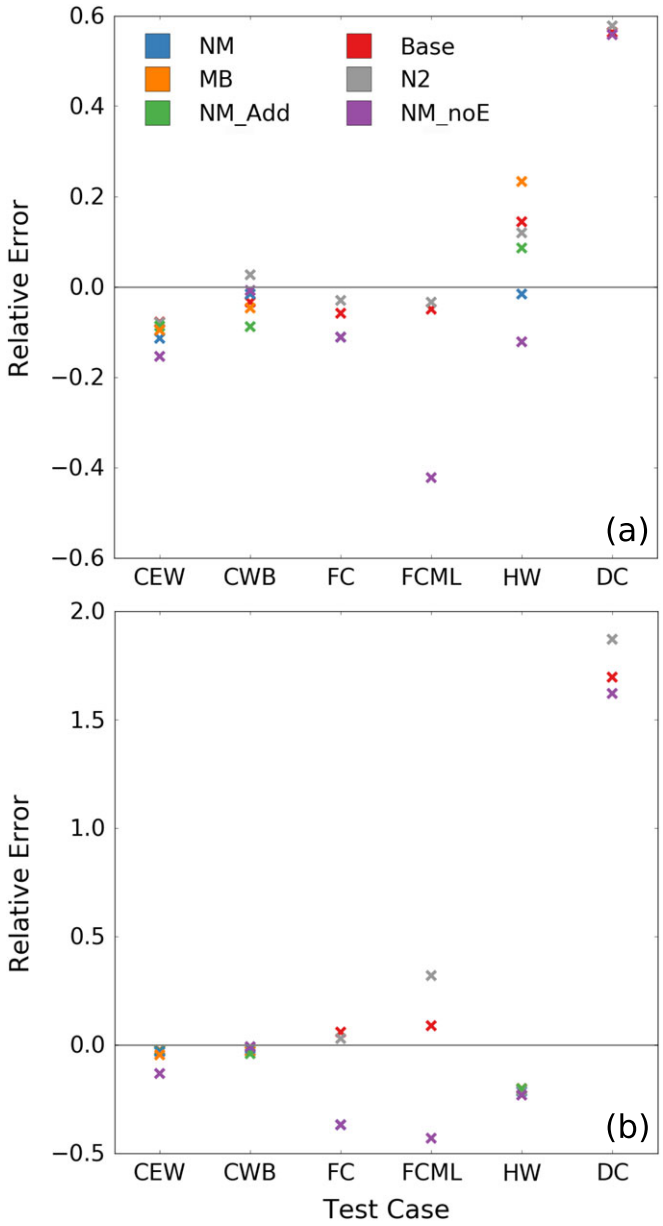

Figure 7. Relative error (equation (34)) averaged over the last day of each test case for a series of K-profile parameterization sensitivity tests. The tests are summarized in Table 6. Each colored marker corresponds to a single sensitivity test. Two vertical grid spacings are shown: (a) 1 m and (b) 10 m. CEW = cooling, evaporation, and wind; CWB = cooling with background shear; DC = diurnal cycle; FC = free convection; FCML = free convection with a mixed layer; HW = heating and wind; NM = no match.

5. Analysis of Default CVMix-KPP OSBL Biases and Possible Remedies

We have conducted a number of sensitivity tests to further examine the biases discussed in the previous section and a few solutions are proposed to remedy some of the biases. The sensitivity tests are summarized in Table 6. Each test is associated with a modification to KPP. Figure 7 presents a summary of these tests via the relative error metric defined in equation (34) for $dz = 1$-m (a) and $dz = 10$-m (b) resolutions. In nearly every case we find that the relative OSBL depth error in the baseline configuration of KPP can be reduced with one of the sensitivity tests. However, there is no single sensitivity test that consistently improves the baseline configuration error. These tests are discussed further in the next sections.

6. Treatment of the Boundary Layer Base

The diagnosed boundary layer depth is dependent on near-surface processes through the surface layer buoyancy and momentum (equation (8)) as well as processes near the boundary layer base. Here we examine KPP sensitivities to the parameterization of diffusivity and its associated entrainment near the boundary layer base.

6.1. Remedying the Shallow Bias Found With Fine Grid Spacing

We revisit how the boundary layer depth is diagnosed to help understand the shallow bias seen in the fine-resolution KPP simulations from section 4.1. We focus on the FC, FCML, and DC tests, in which the KPP boundary layer depth computed according to equation (8) simplifies to

$$\mathrm{Ri}_{\mathrm{crit}} = \frac{h\,\left[b_{\mathrm{sl}} - b(h)\right]}{C\,h\,N_e\,w_*}. \tag{36}$$

To reach this expression, we made use of a simplified definition of the unresolved shear, V_t^2, in which all the constants in equation (17) are subsumed into C. We furthermore assume zero velocity. Hence, for a fixed boundary layer buoyancy, b_{sl}, and surface buoyancy forcing (which fixes w_*), the key means to modify the Richardson number for these simulations is via the entrainment layer stratification as measured by N_e.

6.1.1. A Reformulation of V_t^2 to Reduce the Resolution-Dependent Bias

Increased entrainment layer stratification, which is a region of large stratification (e.g., the region with $d \approx h$ in Figure 2), increases the unresolved turbulent shear, V_t^2 (equation (17)). This increased V_t^2 in turn reduces the bulk Richardson number. The diagnosed boundary layer depth then increases to further enhance mixing. At fine vertical resolution, the stratification varies rapidly in the entrainment layer, suggesting that the KPP boundary layer depth can be very sensitive to the level of stratification used for computing V_t^2.

We identify two ways to approximate the entrainment layer stratification, N_{e}, for the Bulk Richardson number calculation. Danabasoglu et al. (2006) define N_{e} according to

$$N_{\mathrm{e}} = \frac{b(k_{\mathrm{osbl}+1/2}) - b(k_{\mathrm{osbl}-1/2})}{z(k_{\mathrm{osbl}+1/2}) - z(k_{\mathrm{osbl}-1/2})}, \tag{37}$$

where k_{osbl} is the vertical index for the grid cell closest to the OSBL depth. In contrast, as shown in section 2.5.1, N_{e} should be defined one cell shallower in the column (i.e., within the boundary layer as in Figure 2) so that

$$N_{\mathrm{e}} = \frac{b(k_{\mathrm{osbl}-1/2}) - b(k_{osbl-3/2})}{z(k_{\mathrm{osbl}-1/2}) - z(k_{osbl-3/2})}. \tag{38}$$

Yet our tests suggest the following provides a preferable alternative measure of the entrainment layer stratification

$$N_{\mathrm{e}} = \max\left(\frac{b(k_{\mathrm{osbl}+1/2}) - b(k_{\mathrm{osbl}-1/2})}{z(k_{\mathrm{osbl}+1/2}) - z(k_{\mathrm{osbl}-1/2})}, \frac{b(k_{\mathrm{osbl}-1/2}) - b(k_{osbl-3/2})}{z(k_{\mathrm{osbl}-1/2}) - z(k_{osbl-3/2})}\right). \tag{39}$$

This formulation increases N_{e} (and hence V_t^2) at fine vertical grid spacing and prevents a case where $N_{\mathrm{e}} \approx 0$ at coarse spacing (which would lead to a nonrobust calculation of the Richardson number).

In Figure 8, we exhibit the relative error averaged over the final day of each test case using equation (39) for the V_t^2 calculation. The new definition of N_{e} greatly reduces the resolution dependent bias found in the FC test and slightly in the FCML and HW test cases.

In the CEW and CWB tests, the model-predicted shear of horizontal momentum dominates the denominator of equation (8), weakening the sensitivity to V_t^2, and hence N_{e}. In the DC test, the new calculation of N_{e} again only slightly diminishes the resolution-dependent bias during destabilizing surface buoyancy forcing.

In most cases, altering the definition of N_{e} according to equation (39) reduces the OSBL bias relative to LES, although only modestly. Thus, our results suggest that altering N_{e} is a useful, albeit not critical, consideration for KPP configurations.

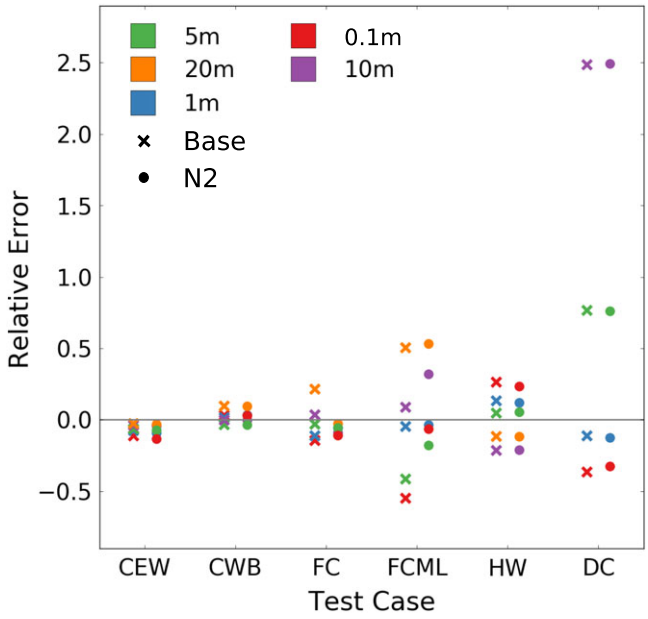

Figure 8. As in Figure 5, but for the N2 sensitivity test (Table 6 and equation (39)). The N2 test is shown as circles, and the base configuration results from Figure 5 are reproduced with an "x." Again the N2 relative error for test DC is above the *y*-axis limit (6.73). CEW = cooling, evaporation, and wind; CWB = cooling with background shear; DC = diurnal cycle; FC = free convection; FCML = free convection with a mixed layer; HW = heating and wind.

6.2. Diffusivity at the Boundary Layer Base

As discussed in section 2.4, there are a number of considerations regarding the matching of interior (below the boundary layer) diffusivities to the diffusivities within the boundary layer. Our results suggest that configurations with (base) and without (no match) matching, with a few critical alterations, can perform well relative to LES. We restrict our analysis in this section to those cases in which the interior shear-driven mixing parameterization is enabled, thus producing a nonzero diffusivity in the interior region below the boundary layer. These tests include the CEW, CWB, and HW configurations.

6.2.1. Considerations for the No Match Configuration

Overall, the simulated OSBL depths from the no match (NM) configuration are similar to the results from the base configuration of KPP (Figure 9), with only a few exceptions. In the CWB test, which simulates a boundary layer deepening into a region of preexisting shear, there is less temporal noise in the simulated OSBL depths in the NM configuration. In the CEW and HW tests, the OSBL depths are slightly shallower than the base configuration of KPP (Figure 9a), although the OSBL depth bias relative to LES improves in the HW test relative to the base configuration. We suggest that the shallower OSBL depths in the NM configuration are partially caused by the inability of interior shear instability-driven mixing to influence the OSBL.

Figure 10 shows the influence of extending the LMD94 shear instability-driven mixing scheme into the OSBL (test NM_Add) for the CEW, CWB, and HW tests. At fine resolution, the CEW and HW OSBL depths (Figures 10a and 10c) increase when shear instability-driven mixing is included in the OSBL. Yet there is no clear improvement in KPP-simulated OSBL depths as the bias relative to LES increases in the HW test but decreases in the CEW test. At coarse resolution, the inclusion of shear instability-driven mixing in the OSBL does not dramatically alter the results. We conjecture that the insensitivity to interior mixing in the OSBL is due to the relatively weak modeled vertical shear of horizontal currents and weakened buoyancy gradients, each resulting from a larger grid spacing d*z*.

In contrast to the CEW and HW tests, the CWB OSBL depth shallows when interior shear instability-driven mixing is added in the OSBL. Further, temporal noise emerges, similar to the base configuration result (see Figure 4 or 9). It is possible that this temporal noise results from the LMD94 shear instability-driven mixing parameterization. The LMD94 scheme is dependent on the gradient Richardson number and can thus be sensitive to grid scale variations in the vertical. Grid scale noise in the gradient Richardson number can lead to noise in the vertical diffusivity and hence the modeled turbulent heat flux, which could cause the temporal

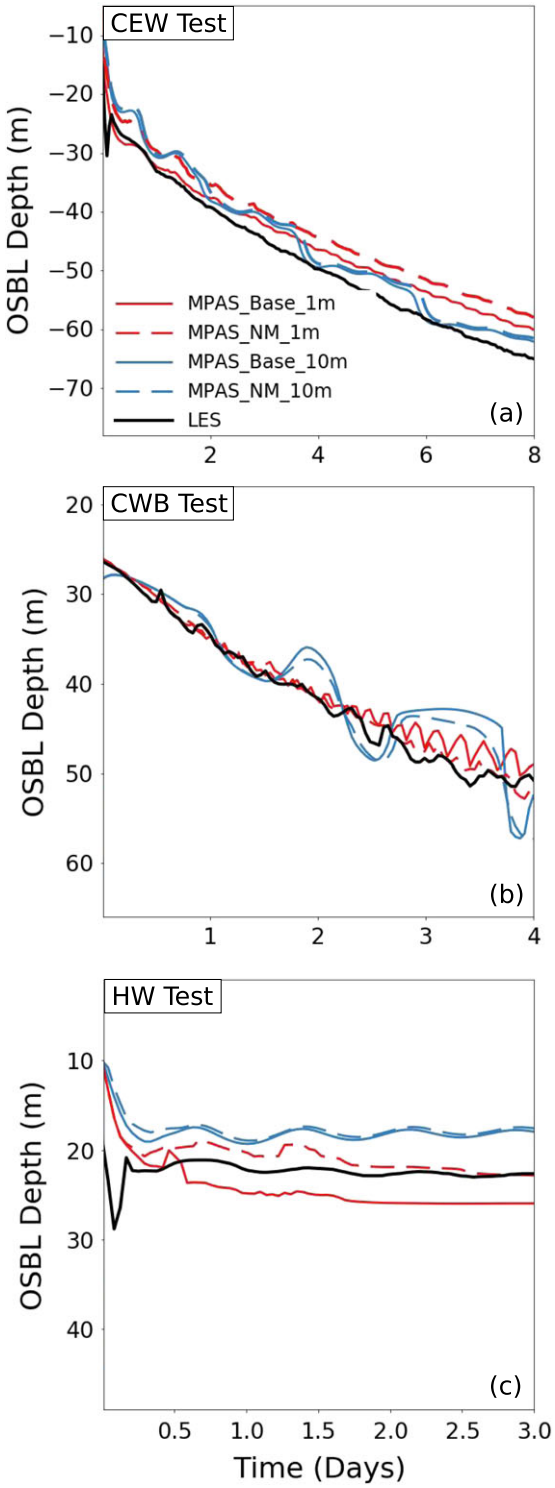

Figure 9. OSBL depths from tests examining the sensitivity of K-profile parameterization to disabling internal matching. (a) CEW test, (b) CWB test, and (c) the HW test. Recall that in the NM configuration, the internal shear-driven mixing parameterization does not influence the boundary layer directly. In every test, the boundary layer depth is calculated following equation (8). CEW = cooling, evaporation, and wind; CWB = cooling with background shear; HW = heating and wind; LES = large eddy simulation; MPAS = Model for Prediction Across Scales; NM = no match; OSBL = ocean surface boundary layer.

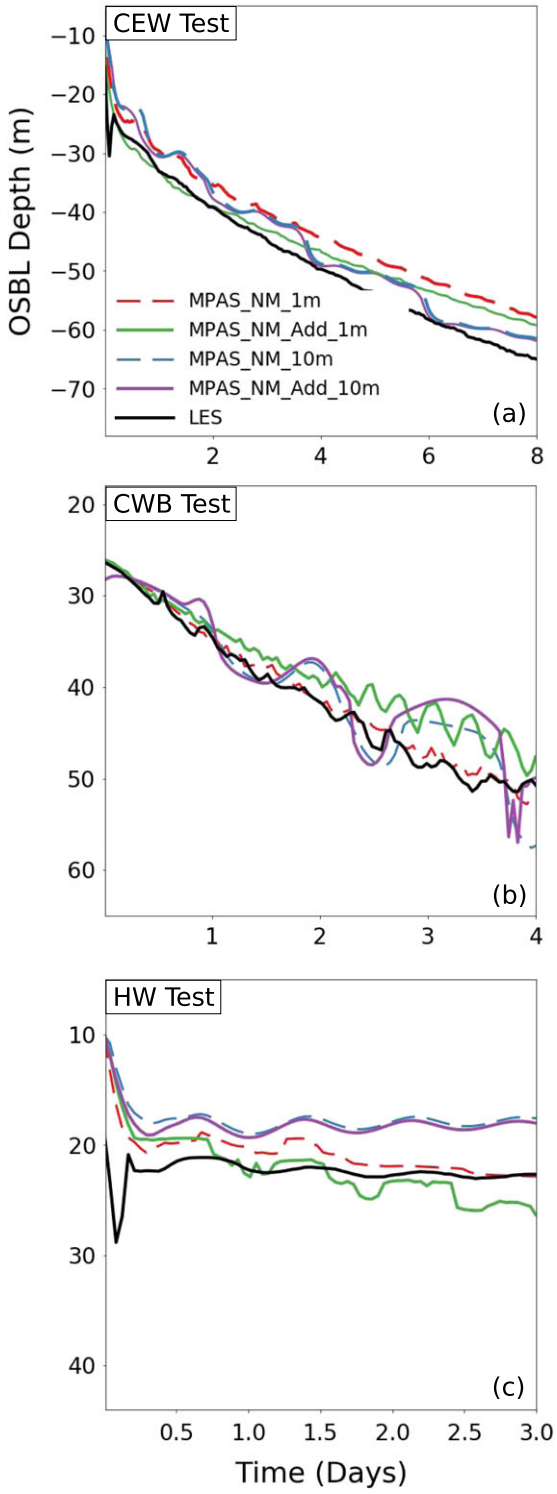

Figure 10. As in Figure 9, but here with the diffusivities and viscosities from the LMD94 interior shear-driven-mixing parameterization added the K-profile parameterization OSBL diffusivities and viscosities. In every test, the boundary layer depth is calculated following equation (8). CEW = cooling, evaporation, and wind; CWB = cooling with background shear; HW = heating and wind; LES = large eddy simulation; MPAS = Model for Prediction Across Scales; NM = no match; OSBL = ocean surface boundary layer.

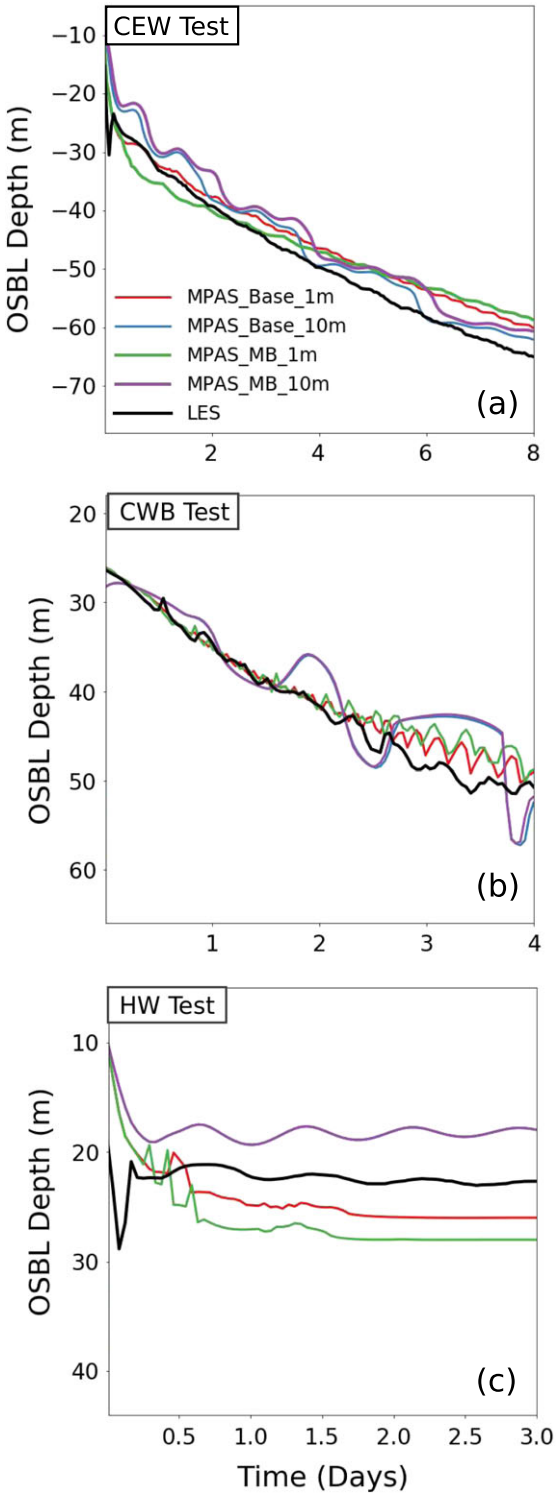

Figure 11. As in Figure 9 but for sensitivity tests matching the gradient of diffusivities across the boundary layer base. CEW = cooling, evaporation, and wind; CWB = cooling with background shear; HW = heating and wind; LES = large eddy simulation; MPAS = Model for Prediction Across Scales; OSBL = ocean surface boundary layer.

noise seen in the CWB test. However, tests where the gradient Richardson number is strongly smoothed in the vertical did not ameliorate the temporal noise.

Overall, KPP simulations with the NM configuration are similar to the base configuration, with only marginally reduced OSBL depth biases. Adding diffusivities from interior mixing schemes (e.g., shear instability) can slightly reduce biases in a few cases (e.g. CEW) but can increase temporal noise and mean biases in the simulated OSBL (CWB test case). Therefore, in the NM configuration we do not recommend adding diffusivities from the shear instability scheme to the KPP diagnosed value. Finally, even though OSBL depths simulated with the NM configuration are similar to the baseline configuration, the NM configuration does not require the added complexities associated with matching diffusivities between the KPP scheme and interior mixing parameterizations. This simplification motivates the NM method.

6.2.2. Considerations for the Base Configuration

Recall that the CVMix base configuration of KPP does not match to gradients of internal diffusivities (Table 1). Sensitivity to this choice is tested in Figure 11. In the CEW and CWB tests there is minimal sensitivity in simulated OSBL depths; however, in the HW test (Figure 11c), matching to internal diffusivity gradients increases the OSBL bias relative to LES at fine grid resolution.

Even though the OSBL bias relative to LES does not strongly increase in the CEW and CWB cases, KPP-simulated momentum and heat fluxes can exhibit sporadic biases relative to LES. Figure 12 shows one such example from the CWB test. When the interior diffusivity and its gradient are matched (MB test), there are brief periods of anomalously strong momentum fluxes (e.g., near day 3 in Figure 12c). When the OSBL deepens into the layer of strong background shear, the interior predicted diffusivities can vary rapidly near the OSBL base and thus strongly influence the KPP OSBL diffusivities. When we match to the interior-predicted diffusivities and viscosities and not the gradients (CVMix default), these regions of vigorous fluxes are strongly damped (compare Figures 12b and 12c). Again, we note that some of the sensitivity seen in Figure 12 may be due in part to the chosen interior shear instability-driven mixing scheme.

Our results (in particular the CWB test) suggest that if diffusivity matching is used, then matching at the boundary layer base should be just to the diffusivities and viscosities. Matching should not occur to the gradients of the diffusivities.

6.3. Examining the Influence of the LMD94 Enhanced Diffusivity Parameterization

LMD94 describe the enhanced diffusivity parameterization (section 2.5.2) as a method to overcome a shallow bias and boundary layer staircase structures commonly found at coarse resolution. Thus, the enhanced diffusivity parameterization is an attempt to increase the effective vertical resolution for a given grid spacing in a highly nonlinear region. Accordingly, it has a much larger effect at coarse resolution. Figure 13 shows boundary layer depths for a subset of our test cases without the enhanced diffusivity parameterization. When the enhanced diffusivity parameterization is disabled, the coarse-resolution OSBL depth shallows and strong temporal noise develops. However, note that prior to the development of temporal noise, the resolution dependence in the FC test case (Figure 13a) is greatly reduced.

The influence of the enhanced diffusivity parameterization on the resolution-dependent bias (section 4.1) is examined in more detail in Figure 14, which shows the time-averaged relative error in OSBL depths (equation (34)) across a wide range of vertical grid spacings ($dz = 0.1$ m to $dz = 20$ m) for each test case. When the enhanced diffusivity parameterization is disabled the resolution dependence is decreased in most test cases. However, the mean relative error (averaged across all tested resolutions) decreases in many test cases, which implies a shallow OSBL bias relative to LES.

These results suggest that the enhanced diffusivity parameterization is partially responsible for the observed resolution dependence for KPP simulated OSBL depths (Figure 5). However, the enhanced diffusivity parameterization is necessary to provide sufficient entrainment in order to prevent temporal noise in OSBL depths but is an incomplete representation of unresolved entrainment across resolutions and surface forcing. We further discuss the temporal noise issue in light of the nonlocal tracer transport parameterization in the next section.

7. Nonlocal Transport in KPP

We now focus on the parameterized nonlocal tracer transport. The KPP nonlocal transport is enabled only under destabilizing surface buoyancy forcing. Across most test cases, the parameterized nonlocal transport behaves well. Yet our experiments also suggest possibilities for extensions warranting further research.

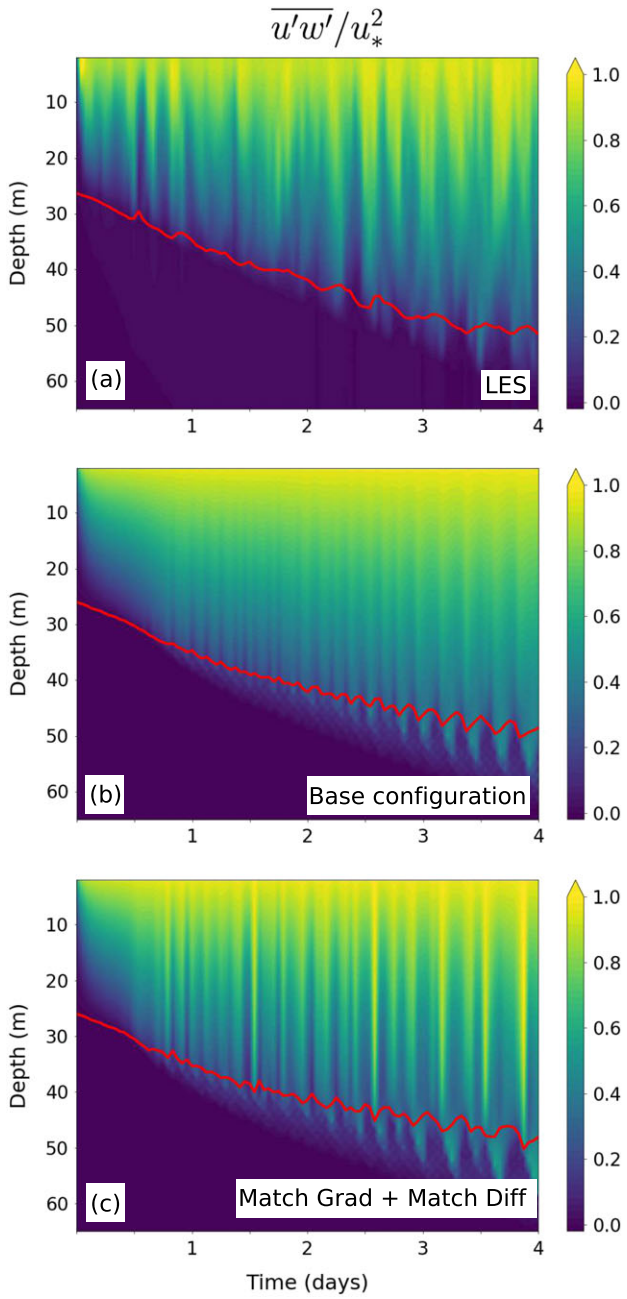

Figure 12. Test case cooling with background shear: Turbulent momentum flux normalized by the surface friction velocity (a–c). The LES results, which are the sum of subgrid and resolved fluxes, are the top row; the middle row is the base configuration; and the bottom row is a test where matching is between the boundary layer and interior diffusivity value and gradient. For K-profile parameterization simulations, the turbulent fluxes are computed via the parameterizations in equations (5), (6), and (20). In every plot, the red line is the boundary layer depth computed via equation (8). LES = large eddy simulation.

7.1. Nonlocal Tracer Transport

In KPP, the nonlocal tracer transport derives from the buoyant production term in the turbulent buoyancy flux equation (see section 2.6.1) and is only nonzero in the presence of a nonzero surface tracer flux. To examine this assumption, we consider the budget for the turbulent salinity flux (equation (22)). Figure 15 shows the budget terms from the FCML LES test case. Note that the sum of the tendency terms is not exactly 0, most likely due to the lack of inclusion of subgrid scale turbulent flux tendencies in equation (22) (Mironov, 2001).

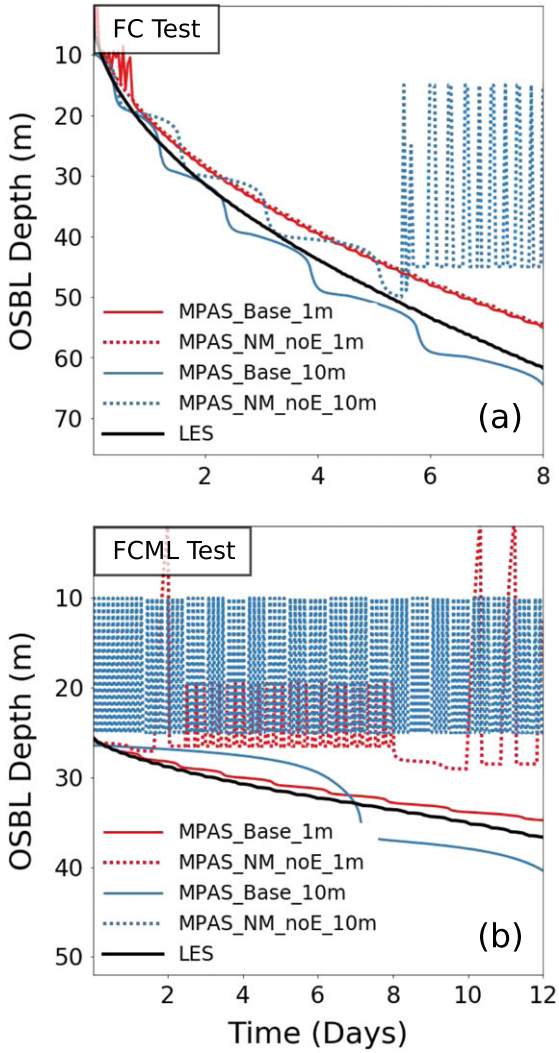

Figure 13. Boundary layer depth sensitivity to the enhanced diffusivity parameterization in the NM configuration. The LES output is dashed black. All OSBL depths are computed using equation (8). (a) The FC test and (b) the FCML test. In panel (b) we have only plotted every other time value of the OSBL depth for visualization. FC = free convection; FCML = free convection with a mixed layer; LES = large eddy simulation; MPAS = Model for Prediction Across Scales; NM = no match; OSBL = ocean surface boundary layer.

Figure 15 shows that the buoyant production of the turbulent salinity flux is larger in magnitude than the local production of the turbulent salinity flux in the OSBL, which implies that the KPP formulation of nonlocal tracer transport is incomplete.

FC sensitivity tests show that if the KPP-parameterized entrainment is too weak, then the OSBL oscillates rapidly (Figure 13a) in time due to an interaction with the nonlocal temperature flux parameterization. This spurious behavior is mitigated by the enhanced diffusivity parameterization, which increases entrainment at the OSBL base. However, for shallow OSBL depths at fine resolution, temporal noise is evident even with the enhanced diffusivity parameterization enabled (Figure 4a).

A parameterization similar to Noh et al. (2003) could replace the enhanced diffusivity parameterization of LMD94 and perhaps reduce the resolution dependence seen in predicted OSBL depths given that there is no explicit consideration of grid resolution in the Noh et al. (2003) parameterization. An improved entrainment heat flux could reduce the interaction with the nonlocal tracer flux parameterization seen in the FC and FCML tests.

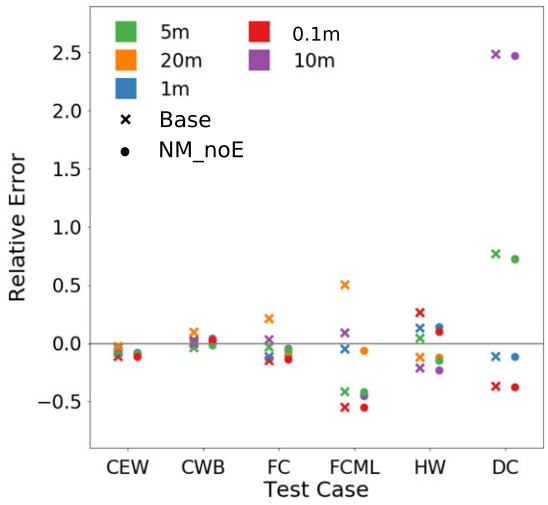

Figure 14. Relative error (equation (34)) averaged over the final day of the simulation for the base configuration (Table 1), xs and sensitivity tests with enhanced diffusivity disabled. Note that in the FC test case, we have averaged over the 24 hr preceding the onset of temporal noise in the coarse-resolution simulation. CEW = cooling, evaporation, and wind; CWB = cooling with background shear; DC = diurnal cycle; FC = free convection; FCML = free convection with a mixed layer; HW = heating and wind; NM = no match.

7.2. Nonlocal Momentum Transport

In the CEW test, a vertical gradient of the vertical flux of meridional momentum was observed in LES in the presence of well-mixed meridional momentum profiles (not shown). This result suggests nonlocal momentum transport could be important. To include a nonlocal momentum transport in KPP, we could use the form suggested by Smyth et al. (2002). We are unaware of published tests of this parameterization in a calling model. Further, it is important to include enhancement due to Langmuir turbulence in any nonlocal momentum transport parameterization. Previous works (Li et al., 2015; McWilliams & Sullivan, 2000; Reichl et al.,

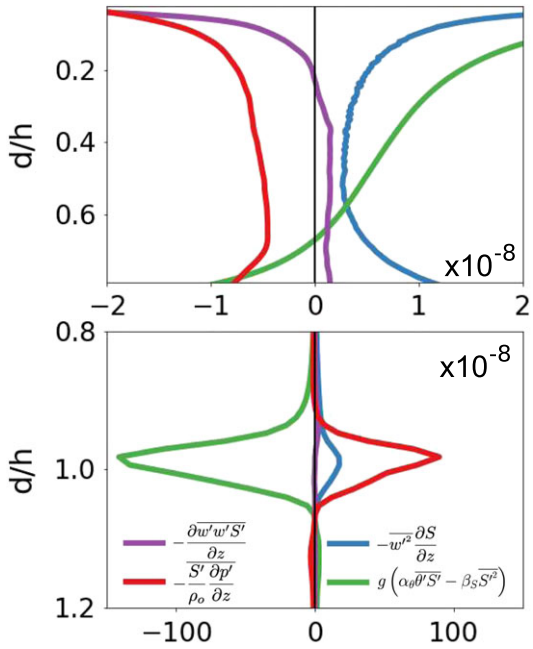

Figure 15. Test case free convection with a mixed layer: budget terms for the turbulent salinity flux equation (see equation (22)) diagnosed from large eddy simulation. The red line is the pressure-salinity covariance, the green line is the buoyant production term, the blue line is the local production term, and the purple line is the triple moment term. The data have been averaged over the final 12 hr of day 12. The two panels span the entire boundary layer, but the *x* range in the upper ocean surface boundary layer is tightened to better elucidate the profiles.

2016) have suggested parameterizations for the influence of Langmuir turbulence on the local diffusivity in KPP, but a nonlocal momentum parameterization that includes Langmuir turbulence has not been proposed for the global ocean (Sinha et al., 2015, proposed a nonlocal momentum transport for Langmuir turbulence associated with full depth Langmuir cells).

8. Conclusions and Best Practice Recommendations

In this paper, we investigated the behavior of the KPP boundary layer parameterization as implemented within the CVMix package (Griffies et al., 2015). The KPP scheme was rigorously tested against a series of horizontally averaged LESs. While many different implementations of KPP have been tested in a number of circumstances, for example, observations (e.g., LMD94, Mukherjee & Tandon, 2016; Van Roekel & Maloney, 2012; Zedler et al., 2002), large-scale ocean simulations (e.g., Li et al., 2001), and against limited LES (e.g., Large & Gent, 1999; McWilliams & Sullivan, 2000; Noh et al., 2016; Reichl et al., 2016; Smyth et al., 2002), it has not been subject to testing against a series of tightly controlled LES cases such as presented in this paper. Our tests focused on implementation choices related just to vertical physics under simplified surface forcing. The tests do not consider the influence of horizontal processes. Horizontal processes represent an important and active (e.g., Bachman et al., 2017; Hamlington et al., 2014) direction for future evaluation of KPP.

8.1. Summary of Main Results and Recommendations

Our tests focused on four main components of KPP physical and numerical choices: vertical resolution and time stepping (sections 2.7 and 4), internal matching (sections 2.4 and 6.2), entrainment at the OSBL base as represented by the enhanced diffusivity parameterization (sections 2.5 and 6.3), and nonlocal transport (sections 2.6 and 7). We here summarize key findings as well as potential solutions.

- MODEL CHOICES:
  - The CVMix implementation appears robust across ocean circulation models given that we tested it within three very different calling models that yielded similar results (Figure 4).
  - KPP is sensitive to the vertical grid spacing (Figure 5). Using the base configuration (Table 1) KPP does not converge to the LES or analytic solutions in the FC test case. Using equation (39) for the V_t^2 parameterization mitigates some of this resolution dependence (Figure 8).
  - KPP is robust to variation in time step (Figure 6).
- NONLOCAL TRANSPORT:
  - Without a sufficient entrainment buoyancy flux, either from the enhanced diffusivity parameterization or our reformulation of the V_t^2 parameterization, then the KPP-simulated OSBL depths can exhibit large and unphysical temporal oscillations (Figure 13).
  - Results from the FCML test case suggest that a nonlocal transport based only on surface fluxes is not sufficient (Figure 15). We suggest that a nonlocal redistribution of the entrainment buoyancy flux should be explored.
- TREATMENT AT THE BOUNDARY LAYER BASE:
  - We have tested values $\mathrm{Ri}_{\mathrm{crit}}(dz)$ between 0.25 and 1.0. In cases with no currents, there is no dependence, given the rapid variation of $\mathrm{Ri}_{\mathrm{crit}}(dz)$ across the OSBL base. For simplicity, we recommend choosing a single value of $\mathrm{Ri}_{\mathrm{crit}}$ across most resolutions.
  - KPP simulates entrainment buoyancy fluxes in two ways. At fine resolution, the entrainment fluxes are sensitive to the V_t^2 parameterization (Figure 4). Use of equation (39) in the V_t^2 parameterization reduces this sensitivity (Figure 8). At coarse resolution, entrainment strength is determined by the enhanced diffusivity parameterization. In a number of tests this parameterization caused a bias that grew as resolution coarsened (Figure 14).
  - For shallow boundary layers and at fine resolution (e.g., the DC test case), high-frequency OSBL depth noise develops (Figure 4c). This noise suggests a lack of simulated entrainment within KPP for this test case.
  - KPP OSBL biases relative to LES are similar for configurations with and without matching boundary layer diffusivities to interior diffusivities (Figure 9). Our results suggest considerations for both configurations of KPP (base and NM) that are summarized here.
    - Matching to interior mixing: Matching to the internal diffusivity and its vertical gradient can lead to noise in the simulated OSBL depths (Figure 11) and periods of anomalously strong fluxes (Figure 12). Therefore, if matching is retained we recommend matching only to the interior diffusivity and not its gradient.
    - No matching: Diffusivities from the LMD94 shear instability parameterization should not be included in the OSBL. Including interior diffusivities in the OSBL reduces the OSBL depth bias slightly in the

Table A1
Symbols Used in This Paper, Along With Preferred Units

Symbol	Description	Units
$\overline{(w'\theta')}_{sfc}$	Surface temperature flux	$m \cdot s^{-1} \cdot K$
$\overline{(w'S')}_{sfc}$	Surface salinity flux	$m \cdot s^{-1} \cdot ppt$
$\overline{(w'b')}_{sfc}$	Surface buoyancy flux	$m \cdot s^{-1} \cdot m \cdot s^{-2}$
h	Ocean boundary layer depth	m
h_e	Depth of the minimum buoyancy flux (entrainment depth)	m
h_m	Depth of the well-mixed layer	m
$\sigma = (-z + \eta)/h$	Boundary layer coordinate	Nondimensional
$\epsilon = 0.1$	Surface layer depth as a percentage of h	Nondimensional
X_{sl}	Surface layer average of X	Dimensions of X
$G(\sigma)$	Shape function for diffusivity profile	Nondimensional
w_x	Turbulent velocity scale of quantity x	m/s
K_x	Parameterized KPP eddy diffusivity for quantity x	m^2/s
Ri_b	Bulk Richardson number	Nondimensional
Ri_{crit}	Critical bulk Richardson number	Nondimensional
V_t^2	Squared unresolved turbulent velocity (in Ri_b)	$m^2 s^{-2}$
γ_x	Nonlocal term	Tracer conc $\times$ m^{-1}
$K_x \gamma_x$	Nonlocal flux	Tracer conc $\times$ m/s
C_*	Strength of nonlocal term	Nondimensional
κ	von Kármán constant	Nondimensional
α_θ	Thermal expansion coefficient	K^{-1}
β_S	Haline contraction coefficient	ppt^{-1}
$\bar{\theta}$	Horizontal mean of temperature	K
$\bar{S}$	Horizontal mean of salinity	ppt
$N^2 \equiv \partial b/\partial z$	Squared buoyancy frequency	s^{-2}
τ	Return to isotropy timescale	s
g	Gravitational acceleration	m/s^2
f	Coriolis parameter	s^{-1}

Note. KPP = K-profile parameterization.

CEW test case (Figures 10a) but introduces temporal oscillations in the OSBL depth in the CWB test case (Figure 10c).

The current configuration of KPP has performed well in many forcing scenarios. However, our results suggest directions for alternative approaches or extensions to KPP to improve model fidelity for several relevant dynamic and thermodynamic situations.

Appendix A : List of Symbols

A summary of selected symbols used in this paper, along with their preferred units, are presented in Table A1.

Appendix B : Elements of the KPP Boundary Layer Scheme

For any prognostic scalar or vector field component ψ (e.g., velocity components and tracer concentrations), the KPP scheme parameterizes the turbulent vertical flux within the surface boundary layer according to

$$\overline{w'\psi'} = -K_\psi \left(\frac{\partial \psi}{\partial z} - \gamma_\psi \right). \tag{B1}$$

In this equation, the eddy diffusivity K_ψ is written as the product of three terms

$$K_\psi = h\, w_\psi(\sigma) G(\sigma). \tag{B2}$$

The boundary layer depth $h > 0$ scales the diffusivity, so that K_ψ is larger for deeper boundary layers. The nondimensional shape function, $G(\sigma)$, is described in B1.

The turbulent velocity scale, $w_\psi \geq 0$, is computed according to

$$w_\psi = \left(\frac{\kappa\, u_*}{\phi_\psi(\sigma h / L)} \right). \tag{B3}$$

In this expression, $\kappa = 0.4$ is the von Kármán constant, $u_* \geq 0$ is the friction velocity scale (determined by the square root of the surface stress magnitude), σ is the nondimensional boundary layer coordinate (see equation (3)), and L is the Obukhov length scale, which is held fixed at its surface value. The function $\phi_\psi \geq 0$ is a nondimensional flux profile that is smaller for negative buoyancy forcing and goes to unity in the absence of buoyancy forcing. Given this form, the velocity scale w_ψ is larger for unstable surface boundary forcing (i.e., negative buoyancy forcing such as when removing heat or adding salt), as well as for stronger mechanical forcing (i.e., larger friction velocity scale as under strong wind forcing).

The KPP vertical viscosity (used for frictional transfer of momentum in the ocean interior) is specified via a separate dimensionless flux profile through the Prandtl number

$$Pr = \left(\frac{K_v}{K_\psi} \right) = \left(\frac{\phi_\psi}{\phi_\mathrm{m}} \right). \tag{B4}$$

See Appendix B of LMD94 as well as Griffies et al. (2015) for full details of the nondimensional flux profile functions ϕ_ψ and ϕ_m, as well as the Obukhov length scale L.

B1. The Nondimensional Shape Function

In the KPP diffusivity expression (equation (B2)), the nondimensional shape function, $G(\sigma)$, is assumed to take a polynomial form proposed by O'Brien (1970)

$$G(\sigma) = c_1 + c_2\sigma + c_3\sigma^2 + c_4\sigma^3, \tag{B5}$$

where c_1, c_2, c_3, and c_4 are constants to be specified by the following considerations. First, since the diffusivity, K_ψ, is assumed to go to 0 at the ocean surface,

$$c_1 = 0. \tag{B6}$$

Within the surface layer ($0 \leq \sigma \leq \epsilon$) (see Figure 1), we can eliminate the gradient of ψ in equation (B1) using Monin-Obukhov similarity theory in the form

$$\frac{\partial \psi}{\partial z} = \left(\frac{\overline{(w'\psi')}_{\mathrm{sfc}}}{\kappa\, z\, u_*} \right) \phi_\psi, \tag{B7}$$

where $\overline{w'\psi'}_{\mathrm{sfc}}$ is the turbulent boundary flux crossing the ocean surface (e.g., turbulent latent and sensible heat, turbulent tracer flux, and turbulent momentum flux). If we combine equations (B1) and (B2) and assume positive surface buoyancy forcing so that the nonlocal term vanishes ($\gamma_\psi = 0$) we have

$$\overline{w'\psi'} = -h\, G\, w_\psi \left(\frac{\partial \psi}{\partial z} \right), \tag{B8}$$

which returns us to the KPP closure form assumed in equation (B1). Now insert equation (B7) into B8, and assume $G(\sigma) \approx \sigma(c_2 + c_3\sigma)$ (valid in the surface layer where $\sigma \leq \epsilon \ll 1$), to yield

$$\overline{w'\psi'} = -\left(\frac{\overline{(w'\psi')}_{\mathrm{sfc}}}{\kappa\, z\, u_*} \right) \phi_\psi\, h\, \sigma\, (c_2 + \sigma c_3)\, w_\psi. \tag{B9}$$

Using equations (B3) and (3) brings equation (B9) to the form

$$\left(\frac{\overline{w'\psi'}}{(\overline{w'\psi'})_{\text{sfc}}} \right) = c_2 + \sigma c_3. \tag{B10}$$

Now we assume a linear decrease of the turbulent flux within the surface layer (i.e., $\overline{w'\psi'}\,\epsilon = \beta\,\overline{w'\psi'}_{\text{sfc}}$, where β is a constant), so that the surface flux at a position σ within the surface layer is given by

$$\left(\frac{\overline{w'\psi'}}{(\overline{w'\psi'})_{\text{sfc}}} \right) = 1 + \frac{\sigma}{\epsilon}(\beta - 1) = c_2 + \sigma\, c_3. \tag{B11}$$

To be valid at $\sigma = 0$ requires

$$c_2 = 1. \tag{B12}$$

To determine the final two shape function coefficients, we require matching across the base of the boundary layer, at $\sigma = 1$. Use of equation (B5) and its derivative at the boundary layer base leads to the following expressions:

$$c_3 = -2 + 3\,G(1) - \left(\frac{\partial G}{\partial \sigma} \right)_{\sigma=1}, \tag{B13a}$$

$$c_4 = 1 - 2\,G(1) + \left(\frac{\partial G}{\partial \sigma} \right)_{\sigma=1}. \tag{B13b}$$

Thus, the shape function is dependent on the chosen boundary conditions at the base of the OSBL. We next consider these boundary conditions.

B2. Diffusivity Matching for the Shape Function at the OSBL Base

LMD94 suggest that the diffusivity and viscosity predicted by KPP, as well as its vertical derivative, should match that predicted by the sum of all mixing parameterizations in the region below the boundary layer (the ocean interior). To ensure appropriate matching, the necessary inputs to equations (B13a) and (B13b) are given by

$$G(\sigma) = \frac{K_\psi^{\text{INT}}(h)}{h\, w_\psi(\sigma)}, \tag{B14a}$$

$$\frac{\partial G}{\partial \sigma} = -\left[\frac{\partial_z K_\psi^{\text{INT}}(h)}{w_\psi(\sigma)} + \frac{K_\psi^{\text{INT}}(h)\partial_\sigma w_\psi(\sigma)}{h\, w_\psi^2(\sigma)} \right], \tag{B14b}$$

where ∂_z and ∂_σ are the partial derivatives with respect to z and σ, respectively, and we evaluate terms on the right-hand side at the boundary layer base, $\sigma = 1$. Without diffusivity matching, the shape function takes the relatively simple cubic form used by Troen and Mahrt (1986):

$$G(\sigma) = \sigma\,(1 - \sigma)^2. \tag{B15}$$

Appendix C: Surface Boundary Fluxes

We detail here the form for vertical turbulent fluxes on the ocean side of the surface boundary. In Large et al. (1994) these surface boundary conditions were formulated for an ocean with a fixed volume, such as for rigid lid ocean models (Bryan, 1969). The rigid lid is rarely used today. We thus provide additional considerations for the nonzero mass flux (Q_{m}) from precipitation, evaporation, river discharge, and melting/freezing of ice.

We frame our discussion by following the finite volume formulation of the tracer equation given by Griffies et al., 2016 (2016; see their equation (L1)), focusing here on just the surface model grid cell affected by advective and nonadvective fluxes from boundary transfer. We define advective transfer as that arising from the transfer of trace matter or heat as part of mass transfer, $Q_{\text{m}} \neq 0$. A surface mass flux carries tracers with concentration ψ_{m} and heat represented by the potential (or conservative) temperature θ_{m}. In contrast, nonadvective transfer arises from radiative and turbulent fluxes not directly associated with Q_{m}, thus changing tracer concentration without changing ocean mass. We base the formulation of turbulent fluxes on the *natural boundary conditions* described by Huang (1993) and Griffies et al. (2001). For simplicity we assume the seawater Boussinesq approximation, thus allowing for density factors to be set to the constant reference density ρ_0. Generalizations to a non-Boussinesq fluid are straightforward.

C1. Formulating the Surface Boundary Condition

The ocean surface boundary fluxes are consistent with the conservation of matter and heat crossing the boundary: What leaves the ocean must enter the atmosphere, land, or ice and vice versa. The vertical tracer flux on the ocean side of the boundary includes the turbulent flux, $\overline{(w'\psi')}_{\text{sfc}}$. Additionally, there is an *advective* flux, $Q_{\text{m}}\,\psi$, that arises from the transfer of water across the boundary with ψ the ocean tracer concentration at the boundary. Our sign convention is chosen so that $Q_{\text{m}} > 0$ for water entering the ocean, whereas $w' > 0$ for an upward turbulent fluctuation within the ocean surface layer. Hence, $\rho_0\,\overline{(w'\psi)'}_{\text{sfc}} - Q_{\text{m}}\,\psi$ is the net upward directed flux at the surface boundary.

The water flux through the ocean surface is continuous. However, it can carry a different tracer concentration on both sides of the ocean surface interface. For example, the salinity of water vapor is 0 so that salt is fully retained in the ocean during evaporation. Similarly, salt is only partly incorporated within sea ice upon transitioning from liquid to solid, with most of the salt returned to the ocean via brine.

C1.1. Boundary Condition for Matter

The above considerations lead to the expression of matter conservation at the ocean surface boundary

$$\rho_0\,\overline{(w'\psi')}_{\text{sfc}} - Q_{\text{m}}\,\psi = Q_{\psi}^{\text{nonadv}} - Q_{\text{m}}\,\psi_{\text{m}}, \tag{C1}$$

where Q_{ψ}^{nonadv} is the flux of ψ not associated with the water flux Q_{m}. We choose signs so that $Q_{\psi}^{\text{nonadv}} > 0$ is a vertically upward transfer of matter away from the ocean. Rearrangement renders the expression for the ocean vertical turbulent tracer flux at the surface

$$\rho_0\,\overline{(w'\psi')}_{\text{sfc}} = Q_{\psi}^{\text{nonadv}} - Q_{\text{m}}\left(\psi_{\text{m}} - \psi\right). \tag{C2}$$

All water flux components (precipitation, evaporation, ice melting and formation, and ice or river discharge) can carry a different tracer concentration $\psi_{\text{m,i}}$. So a more general form of the boundary condition takes the form

$$\rho_0\,\overline{(w'\psi')}_{\text{sfc}} = Q_{\psi}^{\text{nonadv}} - \sum_i Q_{\text{m,i}}\left(\psi_{\text{m,i}} - \psi\right), \tag{C3}$$

where $\sum_i Q_{\text{m,i}} = Q_{\text{m}}$ with the index i running over the different water flux contributions. We make use of the boundary condition C3 for the nonlocal KPP redistribution (section 2.6).

C1.2. Boundary Condition for Heat

Although formulated for matter, a boundary condition similar to equation (C3) also holds for heat. Each water flux component can have a distinct temperature contributing to the advective heat flux contribution. The nonadvective heat flux, $Q_{\theta}^{\text{nonadv}}$, is comprised of latent, sensible, and radiative heat fluxes. There are different latent heat contributions, L_{θ}^{lat}, due to phase transitions between liquid and vapor as well as between liquid and ice. The radiative heat flux consists of two components. Thermal radiation Q_{θ}^{ther} is absorbed in the surface layer and thus contributes to the surface heat flux. In contrast, shortwave radiation Q_{θ}^{sw} penetrates through the surface layer and is absorbed within the water column. Shortwave radiation thus forms a vertically distributed heat source as determined by the vertical radiation extinction profile (e.g., Paulson & Simpson, 1977).

Bringing all terms together leads to the turbulent temperature flux at the ocean surface

$$\rho_0\,\overline{(w'\theta')}_{\text{sfc}} = Q_{\theta}^{\text{sens}} + Q_{\theta}^{\text{ther}} - \sum_i Q_{\text{m,i}}\,L_{\theta,i}^{\text{lat}} - \sum_i Q_{\text{m,i}}\left(\theta_{\text{m,i}} - \theta\right). \tag{C4}$$

Our sign convention is such that $\overline{(w'\theta')}_{\text{sfc}} > 0$ for surface cooling, so that $Q_{\theta}^{\text{sens}} > 0$ and $Q_{\theta}^{\text{ther}} > 0$ cools the ocean surface.

C1.3. Shortwave Radiation and the Nonlocal Parameterization

Of particular interest is how to use the boundary condition C4 for the KPP nonlocal redistribution. As written this boundary flux excludes penetrative shortwave radiation. However, some portion of shortwave radiation is absorbed near the ocean surface and thus may need to be nonlocally redistributed within the OSBL. The amount of shortwave radiation to include in the surface buoyancy forcing is a choice left to the calling model. CVMix returns a nondimensional nonlocal transport and the calling model scales this by the appropriate surface tracer flux.

LMD94 propose to include that portion of shortwave radiation absorbed within the OSBL and thus to add it to the right-hand side of equation (C4). This approach represents an upper limit and, if the OSBL is thick enough, it results in the full deposition of shortwave radiation within the boundary layer, which in turn means that all of the shortwave radiation is redistributed through the nonlocal term. However, a thought experiment with a realistic density equation of state can demonstrate a pitfall to choosing the upper bound suggested by LMD94. Assume brackish surface waters, for example, Baltic Sea, with a sea surface temperature below the temperature of maximum density so that the thermal expansion coefficient is negative. Further, assume that local vertical mixing is small and shortwave radiation is the dominating heat flux. Finally, assume a deep OSBL. In this circumstance solar heating leads to an unstable OSBL, and thus, the nonlocal parameterization is active. With a deep OSBL, all of the incident shortwave radiation is included in the nonlocal tracer transport, which results in a solar heat flux and nonlocal heat flux that exceeds the surface heat flux. Thus, new cold water masses would be generated near the surface that were not present in the water column. In a realistic configuration, this process could lead to the artificial generation of sea ice.

A possible solution to the above problem is to make the strength of the nonlocal flux have a depth dependence and to only include the portion of the shortwave radiation absorbed between the sea surface and a given depth in the nonlocal temperature transport. This approach ensures that the redistributed heat flux is smaller than the total shortwave radiation entering the ocean. It is used in Baltic Sea models based on MOM, Fennel et al. (2010), and Neumann et al. (2017).

Testing this approach in CVMix would require new LES test cases with a realistic equation of state.

C2. Example Turbulent Fluxes

We now consider some examples encountered in ocean and climate modeling.

C2.1. Salinity and Nutrients Away From Sea Ice

The air-sea interface generally has zero transfer of salt (salt transfer from aerosols requires separate consideration), so that the nonadvective salt flux is 0, $Q_S^{\text{nonadv}} = 0$. The salt content of evaporation, precipitation, and river discharge is commonly assumed to be 0, $S_{\text{m}} = 0$, in which case

$$\rho_0 \, \overline{(w'S')}_{\text{sfc}} = Q_{\text{m}} \, S = (P - E + R) \, S. \tag{C5}$$

For ocean models, the surface salinity, S, is generally assumed equal to its value in the top model grid cell. When freshwater is added to the ocean ($P - E + R > 0$), the turbulent salinity flux is positive, $\overline{(w'S')}_{\text{sfc}} > 0$, corresponding to a reduction (dilution) of surface ocean salinity.

As noted by Huang (1993), Griffies et al. (2001), and Olbers et al. (2012), the flux (C5) is the turbulent salinity flux within the ocean surface layer arising from the transfer of freshwater across the ocean surface boundary. It furthermore changes ocean buoyancy through its impact on density. Although it is analogous to the virtual salt flux used in rigid lid models, it is conceptually distinct and thus considered an *equivalent salinity flux* (see equation (2.25) of Olbers et al. (2012)). Namely, the virtual salt flux represents a transfer of salt across the ocean surface rather than a turbulent ocean salinity flux induced by a surface freshwater flux.

For dissolved or suspended tracers, such as nutrients or plankton, a surface boundary condition similar to equation (C5) applies for the KPP nonlocal redistribution. Additionally, for nutrients a nonadvective flux, Q_ψ^{nonadv}, can be added to encompass entrainment of, for example, desert dust.

C2.2. Salinity in the Presence of Sea Ice

A mass flux related to sea ice formation, Q_{freeze}, carries salinity, S_{freeze}, due to the inclusion of salt within the sea ice matrix. Likewise, a meltwater flux, Q_{melt}, has a nonzero salinity, S_{melt}. Another salt flux is brine released from ice cavities upon the formation of sea ice, which can destabilize the water column due to its impact on surface density. The brine release mass flux is Q_{brine}, and brine salinity is S_{brine}. In the presence of sea ice, the complete salinity boundary condition becomes

$$\rho_0 \, \overline{(w'S')}_{\text{sfc}} = (P + R - E) \, S - Q_{\text{freeze}} \left(S_{\text{freeze}} - S \right) - Q_{\text{melt}} \left(S_{\text{melt}} - S \right) - Q_{\text{brine}} \left(S_{\text{brine}} - S \right). \tag{C6}$$

C2.3. A Neutral Boundary Condition for Temperature

In the absence of information regarding the temperature of the various freshwater flux components, we consider a *neutral* assumption whereby the heat content of the freshwater boundary flux does not alter the sea

surface temperature (i.e., the top model grid cell temperature). More generally, a neutral tracer flux changes the tracer content (or heat) of the surface ocean but not its surface concentration. We thus consider the temperature of river runoff, precipitation, and evaporation to be the same as that of the top model grid cell. This choice reduces the temperature boundary condition (C4) to

$$\rho_0 \, \overline{(w'\theta')}_{\text{sfc}} = Q_\theta^{\text{sens}} + Q_\theta^{\text{ther}} - \sum_i Q_{\text{m,i}} \, L_{\theta,i}^{\text{lat}}. \tag{C7}$$

This neutral assumption does not always hold, such as in regions where the temperature in the boundary freshwater flux is different from the sea surface, for example, cold rain over a warm ocean. Furthermore, the neutral approximation must not be applied to nutrient fluxes in ecosystem model applications given the need to avoid spurious nutrient sources.

C3. Buoyancy Boundary Condition

We define buoyancy as

$$b = -\frac{g\,(\rho - \rho_0)}{\rho_0}, \tag{C8}$$

with buoyancy changes arising from change in temperature and salinity

$$g^{-1} \frac{\mathrm{D}b}{\mathrm{D}t} = \alpha_\theta \frac{\mathrm{D}\theta}{\mathrm{D}t} - \beta_S \frac{\mathrm{D}S}{\mathrm{D}t}, \tag{C9}$$

where α_θ is the thermal expansion coefficient and β_S the haline contraction coefficient. At the ocean surface the turbulent vertical flux of buoyancy is given by

$$g^{-1} \, \overline{(w'\, b')}_{\text{sfc}} = \alpha_\theta \, \overline{(w'\, \theta')}_{\text{sfc}} - \beta_S \, \overline{(w'\, S')}_{\text{sfc}}. \tag{C10}$$

The signs are chosen so that $\overline{(w'\, b')}_{\text{sfc}} > 0$ corresponds to a vertically upward turbulent flux of buoyancy, which acts to destabilize the the surface ocean (see Figure 2). In most parts of the ocean, the thermal expansion coefficient is positive, $\alpha_\theta > 0$, with the seasonally fresh and cold Baltic Sea a counterexample. For positive thermal expansion coefficient regions, a destabilizing buoyancy flux arises from surface cooling ($\overline{(w'\, \theta')}_{\text{sfc}} > 0$). A destabilizing buoyancy flux also arises from surface salinification ($\overline{(w'\, S')}_{\text{sfc}} < 0$) with the haline contraction coefficient positive, $\beta_S > 0$.

In CVMix, only the surface buoyancy flux is required to determine the Obukhov length (equation (B3)). The surface salt and heat fluxes, as well as α_θ and β_S, are determined by the calling circulation model. The nonlocal tracer transport computed by CVMix is nondimensional and must be scaled by the surface tracer flux computed by the calling model (see section 2.6).

Appendix D: Salinity Testing in the NCAR LES

To simulate the influence of salinity in the National Center for Atmospheric Research (NCAR) LES model (McWilliams et al., 1997; Sullivan et al., 2007), the influence of salinity on the resolved buoyancy is included via a linear equation of state. Thus, the modified buoyancy term in the vertical momentum equation becomes

$$b = -g \left[1 - \alpha_\theta \left(\theta - \bar{\theta}\right) + \beta_S \left(S - \bar{S}\right)\right], \tag{D1}$$

where the overline indicates a horizontal average. Buoyancy terms in the subgrid TKE scheme are modified in a similar fashion. To test this implementation two buoyant bubble tests were conducted. In both tests, the buoyancy perturbation is initialized via

$$b(x,y,z) = min\left[0, \Delta b \, \cos\left(\frac{\pi\, r(x,y,z)}{2}\right)\right], \tag{D2}$$

where Δb is the maximum buoyancy perturbation and $r(x,y,z)$ is the distance from the bubble center. One test is initialized by a temperature perturbation. For the second test, the salinity is initialized such that in buoyancy the perturbation is identical to the temperature test. The results from this test are shown in Figure D1. The

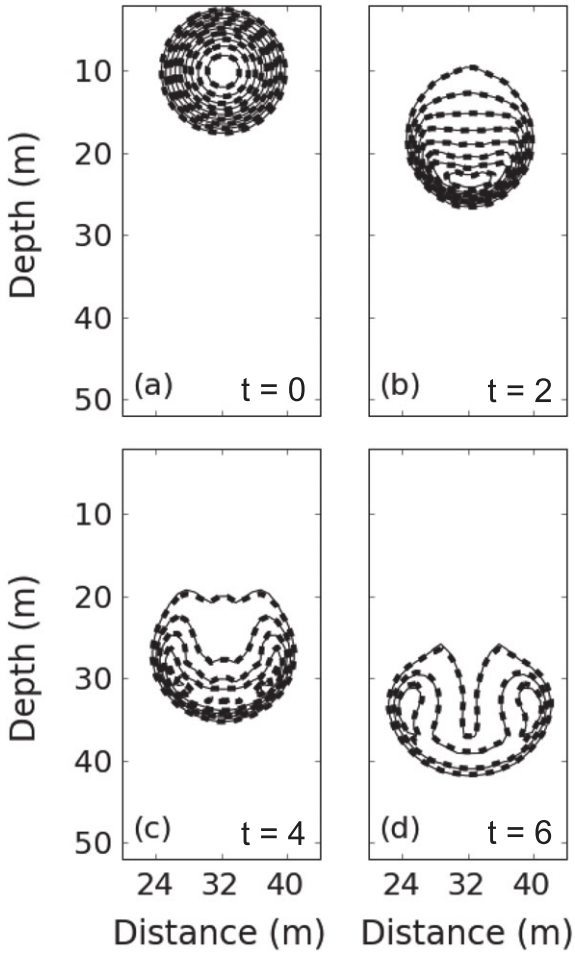

Figure D1. Results from a buoyant bubble test. The thin solid lines are the buoyancy bubble dependent on temperature only. The thicker dashed lines are results from the buoyant bubble dependent on salinity alone. The respective perturbations in temperature and salinity have equivalent buoyancy perturbations. Labels in panels (a)–(d) are the time in minutes from the start of the simulation.

thin solid lines are for the temperature perturbation, and the thick dashed lines are the salinity perturbations. As the two bubbles have identical buoyancy they should fall on top of each other. Following from a to d in Figure D1, the bubbles stay together.

The buoyancy changes and the corresponding salinity flux implementation are validated in a free convection simulation due to surface evaporation (CEW; Table 3). The agreement in the location of the buoyancy flux minimum diagnosed from the LES model and the analytic solution (see Appendix F) is quite good (not shown). Given these results, we have confidence in the comparison of salinity from CVMix to LES for the simulations described in Tables 3 and 4 and sections 4–7.

Appendix E: Form of Solar Radiation

In the LES and single column tests, the shortwave radiation is assumed to obey a Jerlov type IB extinction profile (Paulson & Simpson, 1977). The time variation of incident shortwave radiation (Wm^{-2}; $F_{sw}(t)$) is given as

$$F_{sw}(t) = Q_{sw}^{max} \max\left\{\cos\left[2\pi\left(\frac{t}{T} - \frac{1}{2}\right)\right], 0\right\}, \tag{E1}$$

where t is the time in seconds and $T = 86,400$ are the number of seconds in 1 day. The peak incoming shortwave radiation (Q_{sw}^{max}) is determined by forcing a balance between the daily integrated buoyancy gain and the daily integrated buoyancy loss ($\mathrm{m}^2/\mathrm{s}^3$), that is,

$$\int_0^T \frac{g\,\alpha_\theta}{\rho\,c_p} F_{sw}(t)\,dt = -\int_0^T \overline{w'\,b'}_{sfc}\,dt, \tag{E2}$$

where this equation has been multiplied by the gravitational acceleration, g, and the thermal expansion coefficient, α_θ (equation (29)), and divided by the reference density and $c_p \equiv 4,200 \text{J}\cdot\text{kg}^{-1}\cdot{}^\circ\text{C}^{-1}$ to ensure consistent units. Upon integration, and using equation (E1), the maximum surface shortwave radiation is given as

$$Q_{sw}^{max} = -\pi\left(\frac{\rho\,c_p\overline{w'b'}_{sfc}}{g\,\alpha_\theta}\right). \tag{E3}$$

The units of equation (E3) are $\text{m}\cdot{}^\circ\text{C}\cdot\text{s}^{-1}$ given the division by $g\,\alpha_\theta$.

Appendix F: Analytic Boundary Layer Solution

The derivation in this appendix closely follows previous work (Haine & Marshall, 1998; Turner, 1973), but here we do not assume the entrainment of fluid into the boundary layer is negligible. Assuming that entrainment into the boundary layer is negligible is equivalent to assuming that $h = h_e = h_m$ in KPP (Figure 2). In our derivation we slightly relax this assumption by assuming the buoyancy jump between the boundary layer and interior is large but not a discontinuity (i.e., $h \approx h_e \approx h_m$).

We begin by assuming that a model is forced with a horizontally uniform, constant in time, buoyancy flux, which simplifies the buoyancy equation to

$$\frac{\partial b}{\partial t} = -\frac{\partial \overline{w'b'}}{\partial z}. \tag{F1}$$

Next, equation (F1) is integrated from the surface ($z = 0$) to a depth $-H$ below the boundary layer (h) that does not change in time, that is,

$$\int_{-H}^{0} \frac{\partial b}{\partial t}\,dz = -\int_{-H}^{0} \frac{\partial \overline{w'b'}}{\partial z}\,dz. \tag{F2}$$

Assuming $\overline{w'b'}$ is small at a depth H below the boundary layer, equation (F2) can be written as

$$\frac{\partial}{\partial t}\int_{-H}^{0} b(z)\,dz = -\overline{(w'b')}_{z=0}. \tag{F3}$$

We now assume a buoyancy profile for the upper ocean. The assumed form is shown in Figure F1. The buoyancy is uniform in the boundary layer, the stratification is constant below the boundary layer, and there is a sharp (but not discontinuous) buoyancy change between the well-mixed layer and the interior ocean similar to VanZanten et al., 1999 (1999). The strength of the buoyancy jump is assumed to be equal to the deep ocean buoyancy at the boundary layer base (i.e., $N^2|h|$) multiplied by a small constant (a), which is assumed to be less than 1. With this assumption, the boundary layer buoyancy is

$$b(h) = \Delta b - N^2|h| = (a-1)N^2|h|. \tag{F4}$$

equation (F4) then brings equation (F3) into the form

$$\frac{\partial}{\partial t}\left[\int_{-H}^{-h(t)} N^2\,z\,dz + \int_{-h(t)}^{0}(a-1)N^2\,|h|\,dz\right] = \overline{(w'b')}_{sfc}. \tag{F5}$$

equation (F5) can be integrated to find

$$(1-2a)N^2\frac{\partial}{\partial t}\left[\frac{h^2}{2}\right] = \overline{(w'b')}_{sfc}. \tag{F6}$$

The constant a is determined by using the formula for the boundary layer heat flux from Lilly (1968) and the empirical rule of convection

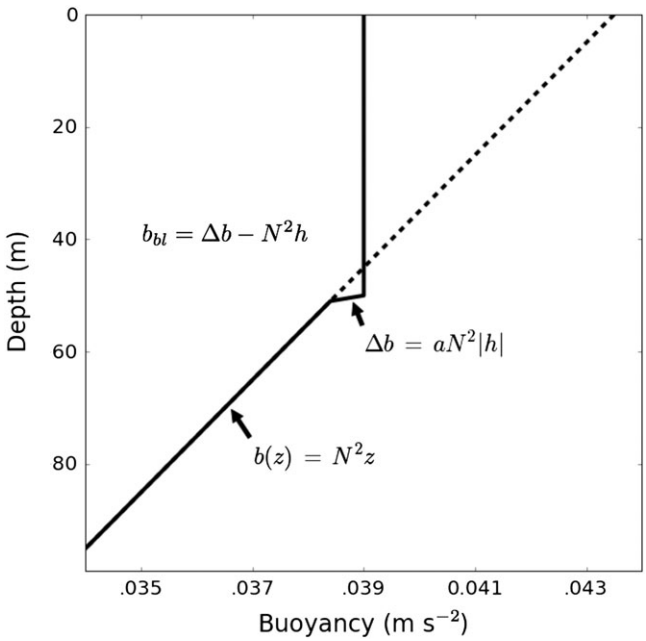

Figure F1. Schematic illustrating the analytic buoyancy solution. The dashed line is the initial stratification, and the solid line is the profile after some time (t). The buoyancy change across the entrainment layer is assumed to be a small fraction of the interior stratification ($a << 1$). Thus, this case does not assume a jump discontinuity between the well-mixed layer and the interior ocean. Yet given that the buoyancy change is large, $h_e \approx h$ (Figure 2).

$$\frac{\overline{(w'b')}(h_e)}{\overline{(w'b')}_{sfc}} \approx 0.2. \tag{F7}$$

Since the buoyancy change is sharp, $h_e \approx h$, and $\overline{(w'b')}(h) \approx \overline{(w'b')}(h_e)$. Equating the empirical rule of convection and the boundary layer heat flux formula from Lilly (1968) yields

$$\overline{(w'b')}(h) = \Delta b \frac{\partial h}{\partial t} = 0.2 \overline{(w'b')}_{sfc}. \tag{F8}$$

Using the assumed form of the entrainment layer buoyancy change, equation (F8) becomes

$$a N^2 |h| \frac{\partial h}{\partial t} = a N^2 \frac{\partial}{\partial t}\left(\frac{h^2}{2}\right) = 0.2 \overline{(w'b')}_{sfc}. \tag{F9}$$

Dividing equation (F9) by equation (F6) gives

$$\frac{a}{1-2a} = 0.2. \tag{F10}$$

Equation (F10) gives $a \approx 0.143$. Inserting this result into equation (F6), the final expression for boundary layer depth is

$$h(t) = \left(\frac{2.8 \overline{(w'b')}_{sfc} t}{N^2}\right)^{1/2}. \tag{F11}$$

Acknowledgments
We thank Scott Bachman, Mark Petersen, Rachel Robey, Milena Veneziani, and Phillip Wolfram for providing very useful comments on earlier drafts of this paper. We thank Baylor Fox-Kemper and four anonymous reviewers for comments that have greatly improved this manuscript. We also thank Mathew Maltrud for help in configuring POP simulations. This research was supported as part of the Energy Exascale Earth System Model (E3SM) project, funded by the U.S. Department of Energy, Office of Science, Office of Biological and Environmental Research. Michael Levy and Brian Kauffman were partially supported by the U.S. Department of Energy, Office of Science, Office of Biological and Environmental Research SciDAC grant DE-SC0012605 to NCAR. NCAR is sponsored by the National Science Foundation. Brandon Reichl was supported through the Cooperative Institute for Climate Science at Princeton University and the Princeton Environmental Institute at Princeton University through the Carbon Mitigation Initiative. This research used resources of the Oak Ridge Leadership Computing Facility at the Oak Ridge National Laboratory, which is supported by the Office of Science of the U.S. Department of Energy under contract DE-AC05-00OR22725 through an ALCC allocation and resources provided by the Los Alamos National Laboratory Institutional Computing Program, which is supported by the U.S. Department of Energy National Nuclear Security Administration under contract DE-AC52-06NA25396. All data required to reconstruct the figures and tables in this paper are publicly available at https://figshare.com/articles/Model_{D}ata_{f}or_{c}omparisons/6712820.

References

Abarbanel, H. D., Holm, D. D., Marsden, J. E., & Ratiu, T. (1984). Richardson number criterion for the nonlinear stability of three-dimensional stratified flow. *Physical Review Letters*, *52*(26), 2352.

Adcroft, A. J., Hallberg, R. W., & MOM6 Team (2018). MOM6 source code and documentation, GFDL Ocean Group Technical Report.

Ayotte, K. W., Sullivan, P. P., Andren, A., Doney, S. C., Holtslag, A. A. M., Large, W. G., et al. (1996). An evaluation of neutral and convective planetary boundary-layer parameterizations relative to large eddy simulations. *Boundary-Layer Meteorology*, *79*, 131–175.

Bachman, S., Fox-Kemper, B., Taylor, J., & Thomas, L. (2017). Parameterization of frontal symmetric instabilities. I: Theory for resolved fronts. *Ocean Models*, *109*, 72–95.

Barad, M. F., & Fringer, O. B. (2010). Simulations of shear instabilities in interfacial gravity waves. *Journal of Fluid Mechanics*, *644*, 61–95.
Brown, A. R. (1996). Evaluation of parametrization schemes for the convective boundary layer using large-eddy simulation results. *Boundary-Layer Meteorology*, *81*(2), 167–200.
Bryan, K. (1969). A numerical method for the study of the circulation of the world ocean. *Journal of Computational Physics*, *4*, 347–376.
Burchard, H., & Bolding, K. (2001). Comparative analysis of four second-moment turbulence closure models for the oceanic mixed layer. *Journal of Physical Oceanography*, *31*(8), 1943–1968.
Canuto, V. M., Cheng, Y., & Howard, A. M. (2007). Non-local ocean mixing model and a new plume model for deep convection. *Ocean Models*, *16*(1-2), 28–46.
Canuto, V. M., Howard, A., Cheng, Y., & Dubovikov, M. S. (2001). Ocean turbulence. Part I: One-point closure model-momentum and heat vertical diffusivities. *Journal of Physical Oceanography*, *31*(6), 1413–1426.
Danabasoglu, G., Large, W. G., Tribbia, J. J., Gent, P. R., Briegleb, B. P., & McWilliams, J. C. (2006). Diurnal coupling in the tropical oceans of CCSM3. *Journal Climate*, *19*(11), 2347–2365.
Deardorff, J. W. (1966). The counter-gradient heat flux in the lower atmosphere and laboratory. *Journal of the Atmospheric Sciences*, *23*, 503–506.
Deardorff, J. W. (1970). Convective velocity and temperature scales for the unstable planetary boundary layer and for Rayleigh convection. *Journal of the atmospheric sciences*, *27*(8), 1211–1213.
Deardorff, J. W. (1972). Theoretical expression for countergradient vertical heat-flux. *Journal of Geophysical Research*, *77*(30), 5900–5904.
Deardorff, J. W. (1980). Stratocumulus-capped mixed layers derived from a three-dimensional model. *Boundary-Layer Meteorology*, *18*(4), 495–527.
Ertel, H. (1942). The vertical turbulent heat flux in the atmosphere. *Meteorologische Zeitschrift*, *59*, 250–253.
Fennel, W., W., Radtke, H., Schmidt, M., & Neumann, T. (2010). Transient upwelling in the central Baltic Sea. *Continental Shelf Research*, *30*(19), 2015–2026.
Gaspar, P. (1988). Modeling the seasonal cycle of the upper ocean. *Journal of Physical Oceanography*, *18*(2), 161–180.
Griffies, S. M., Danabasoglu, G., Durack, P. J., Adcroft, A. J., Balaji, V., Böl̀ning, C. W., et al. (2016). Omip contribution to cmip6: Experimental and diagnostic protocol for the physical component of the ocean model intercomparison project. *Geoscientific Model Development*, *9*, 3231–3296. https://doi.org/10.5194/gmd-9-3231-2016
Griffies, S. M., Levy, M., Adcroft, A. J., Danabasoglu, G., Hallberg, R. W., Jacobsen, D., et al. (2015). Theory and numerics of the Community Ocean Vertical Mixing (CVMix) Project, available from https://github.com/CVMix/CVMix-description, Tech. rep.
Griffies, S. M., Pacanowski, R. C., Schmidt, R. M., & Balaji, V. (2001). Tracer conservation with an explicit free surface method for z-coordinate ocean models. *MWR*, *129*, 1081–1098.
Haine, T. W., & Marshall, J. (1998). Gravitational, symmetric, and baroclinic instability of the ocean mixed layer. *Journal of Physical Oceanography*, *28*(4), 634–658.
Hallberg, R. W (2003). The suitability of large-scale ocean models for adapting parameterizations of boundary mixing and a description of a refined bulk mixed layer model. In P. Müller & C. Garrett (Eds.), *Near-Boundary Processes and Their Parameterization* (pp. 187–203). University of Hawaii at Manoa: Proceedings of the 13th 'Aha Huliko'a Hawaiian Winter Workshop.
Hamlington, P. E., Van Roekel, L. P., Fox-Kemper, B., Julien, K., & Chini, G. P. (2014). Langmuir–submesoscale interactions: Descriptive analysis of multiscale frontal spindown simulations. *Journal of Physical Oceanography*, *44*(9), 2249–2272.
Harcourt, R. R. (2015). An improved second-moment closure model of Langmuir turbulence. *Journal of Physical Oceanography*, *45*(1), 84–103.
Holtslag, A. A. M., & Moeng, C.-H. (1991). Eddy diffusivity and countergradient transport in the convective atmospheric boundary layer. *Journal of the Atmospheric Sciences*, *48*(14), 1690–1698.
Huang, R. X. (1993). Real freshwater flux as a natural boundary condition for the salinity balance and thermohaline circulation forced by evaporation and precipitation. *Journal of Physical Oceanography*, *23*, 2428–2446.
Johnson, G. C., Sloyan, B. M., Kessler, W. S., & McTaggart, K. E. (2002). Direct measurements of upper ocean currents and water properties across the tropical pacific during the 1990s. *Progress in Oceanography*, *52*(1), 31–61.
Kantha, L. H., & Clayson, C. A. (1994). An improved mixed layer model for geophysical applications. *Journal of Geophysical Research*, *99*(C12), 25,235–25,266.
Kato, H., & Phillips, O. (1969). On the penetration of a turbulent layer into stratified fluid. *Journal of Fluid Mechanics*, *37*(4), 643–655.
Kraus, E. B., & Turner, J. S. (1967). A one-dimensional model of the seasonal thermocline II. The general theory and its consequences. *Tellus*, *19*(1), 98–106.
Lappen, C.-L., & Randall, D. A. (2001). Toward a unified parameterization of the boundary layer and moist convection. part i: A new type of mass-flux model. *Journal of the Atmospheric Sciences*, *58*(15), 2021–2036.
Large, W. G., & Gent, P. R. (1999). Validation of vertical mixing in an equatorial ocean model using large eddy simulations and observations. *Journal of Physical Oceanography*, *29*, 449–464.
Large, W. G., McWilliams, J. C., & Doney, S. C. (1994). Oceanic vertical mixing: A review and a model with a nonlocal boundary layer parameterization. *Reviews of Geophysics*, *32*(4), 363–403.
Lemarié, F., Debreu, L., Madec, G., Demange, J., Molines, J.-M., & Honnorat, M. (2015). Stability constraints for oceanic numerical models: Implications for the formulation of time and space discretizations. *Ocean Modelling*, *92*, 124–148.
Lemarié, F., Kurian, J., Shchepetkin, A. F., Molemaker, M. J., Colas, F., & McWilliams, J. C. (2012). Are there inescapable issues prohibiting the use of terrain-following coordinates in climate models? *Ocean Modelling*, *42*, 57–79.
Li, X., McWilliams, J., & Fu, L.-L. (2001). A Comparison of two vertical-mixing schemes in a Pacific Ocean General Circulation Model. *Monthly Weather Review*, *14*, 1377–1398.
Li, Q., Webb, A., Fox-Kemper, B., Craig, A., Danabasoglu, G., Large, W. G., & Vertenstein, M. (2015). Langmuir mixing effects on global climate: WAVEWATCH III in CESM. *Ocean Models*, *103*, 145–160.
Lilly, D. K. (1968). Models of cloud-topped mixed layers under a strong inversion. *Quarterly Journal of the Royal Meteorological Society*, *94*(401), 292–309.
Mailhot, J., & Benoit, R. (1982). A finite-element model of the atmospheric boundary layer suitable for use with numerical weather prediction models. *Journal of the Atmospheric Sciences*, *39*, 2249–2266.
McGrath-Spangler, E. L., Molod, A., Ott, L. E., & Pawson, S. (2015). Impact of planetary boundary layer turbulence on model climate and tracer transport. *Atmospheric Chemistry and Physics*, *15*(13), 7269–7286.
McWilliams, J. C., & Sullivan, P. P. (2000). Vertical mixing by Langmuir Circulations. *Spill Science & Technology Bulletin*, *6*(3-4), 225–237.
McWilliams, J. C., Sullivan, P. P., & Moeng, C.-H. (1997). Langmuir turbulence in the ocean. *Journal of Fluid Mechanics*, *334*, 1–30.

Mellor, G. L., & Yamada, T. (1982). Development of a turbulence closure model for geophysical fluid problems. *Reviews of Geophysics*, *20*(4), 851–875.
Miles, J. W. (1961). On the stability of heterogeneous shear flows. *Journal of Fluid Mechanics*, *10*(04), 496–508.
Mironov, D. V. (2001). Pressure-potential-temperature covariance in convection with rotation. *Quarterly Journal of the Royal Meteorological Society*, *127*(571), 89–110.
Moeng, C.-H., & Sullivan, P. P. (1994). A comparison of shear- and buoyancy-driven planetary boundary layer flows. *Journal of the Atmospheric Sciences*, *51*(7), 999–1022.
Moeng, C.-H., & Wyngaard, J. C. (1984). Statistics of conservative scalars in the convective boundary layer. *Journal of the Atmospheric Sciences*, *41*(21), 3161–3169.
Moeng, C.-H., & Wyngaard, J. C. (1986). An analysis of closures for pressure-scalar covariances in the convective boundary layer. *Journal of the Atmospheric Sciences*, *43*, 2499–2513.
Mukherjee, S., & Tandon, A. (2016). Comparison of the simulated upper-ocean vertical structure using 1-dimensional mixed-layer models. *Ocean Science Discussions*, *2016*, 1–22. https://doi.org/10.5194/os-2016-45
Neumann, T., Radtke, H., & Seifert, T. (2017). On the importance of major baltic inflows for oxygenation of the central Baltic Sea. *Journal of Geophysical Research: Oceans*, *122*, 1090–1101. https://doi.org/10.1002/2016jc012525
Niiler, P. P. (1977). One-dimensional models of the upper ocean. In Modelling and Prediction of the Upper Layers of the Ocean (pp. 143–172). Oxford: Pergamon Press.
Noh, Y., Cheon, W. G., Hong, S. Y., & Raasch, S. (2003). Improvement of the K-profile model for the planetary boundary layer based on large eddy simulation data. *Boundary-Layer Meteorology*, *107*(2), 401–427.
Noh, Y., Ok, H., Lee, E., Toyoda, T., & Hirose, N. (2016). Parameterization of Langmuir circulation in the ocean mixed layer model using LES and its application to the OGCM. *Journal of Physical Oceanography*, *46*(1), 57–78.
O'Brien, J. J. (1970). A note on the vertical structure of the eddy exchange coefficient in the Planetary Boundary Layer. *Journal of the Atmospheric Sciences*, *27*, 1213–1215.
Olbers, D., Willebrand, J., & Eden, C. (2012). *Ocean Dynamics*. Berlin: Springer.
Paulson, C. A., & Simpson, J. J. (1977). Irradiance measurements in the upper ocean. *Journal of Physical Oceanography*, *7*(6), 952–956.
Price, J. F., Weller, R. A., & Pinkel, R. (1986). Diurnal cycling: Observations and models of the upper ocean response to diurnal heating, cooling, and wind mixing. *Journal of Geophysical Research*, *91*(C7), 8411–8427.
Reffray, G., Bourdalle-Badie, R., & Calone, C. (2015). Modelling turbulent vertical mixing sensitivity using a 1-D version of NEMO. *Geoscientific Model Development*, *8*(1), 69–86.
Reichl, B. G., Wang, D., Hara, T., Ginis, I., & Kukulka, T. (2016). Langmuir turbulence parameterization in tropical cyclone conditions. *Journal of Physical Oceanography*, *46*(3), 863–886.
Ringler, T., Petersen, M., Higdon, R. L., Jacobsen, D., Jones, P. W., & Maltrud, M. (2013). A multi-resolution approach to global ocean modeling. *Ocean Models*, *69*, 211–232.
Seidel, D. J., Ao, C. O., & Li, K. (2010). Estimating climatological planetary boundary layer heights from radiosonde observations: Comparison of methods and uncertainty analysis. *Journal of Geophysical Research*, *115*, D16113.
Sinha, N., Tejada-Mart, A. E., Akan, C., & Grosch, C. E. (2015). Toward a k-profile parameterization of langmuir turbulence in shallow coastal shelves. *Journal of Physical Oceanography*, *45*(12), 2869–2895.
Smith, R., Jones, P., Briegleb, B., Bryan, F., Danabasoglu, G., Dennis, J., et al. (2010). The Parallel Ocean Program (POP) reference manual ocean component of the Community Climate System Model (CCSM) and Community Earth System Model (CESM).
Smyth, W. D., Skyllingstad, E. D., Crawford, G. B., & Wijesekera, H. (2002). Nonlocal fluxes and Stokes drift effects in the K-profile parameterization. *Ocean Dynamics*, *52*(3), 104–115.
Soares, P., Miranda, P., Siebesma, A., & Teixeira, J. (2004). An eddy-diffusivity/mass-flux parametrization for dry and shallow cumulus convection. *Quarterly Journal of the Royal Meteorological Society*, *130*(604), 3365–3383.
Stull, R. B. (1993). Review of non-local mixing in turbulent atmospheres: Transilient turbulence theory. *Boundary-Layer Meteorology*, *62*(1), 21–96.
Stull, R. B (2012). *An introduction to boundary layer meteorology*. Berlin, Germany: Springer Science & Business Media.
Sullivan, P. P., McWilliams, J. C., & Melville, W. K. (2007). Surface gravity wave effects in the oceanic boundary layer: Large-eddy simulation with vortex force and stochastic breakers. *Journal of Fluid Mechanics*, *593*, 405–452.
Troen, I. B., & Mahrt, L. (1986). A simple model of the atmospheric boundary layer; sensitivity to surface evaporation. *Boundary-Layer Meteorology*, *37*(1-2), 129–148.
Troy, C. D., & Koseff, J. R. (2005). The instability and breaking of long internal waves. *Journal of Fluid Mechanics*, *543*, 107–136.
Turner, J. (1973). *Bouyancy effects in fluids*. Cambridge: Cambridge University Press.
Umlauf, L., & Burchard, H. (2005). Second-order turbulence closure models for geophysical boundary layers. A review of recent work. *Continental Shelf Research*, *25*(7-8), 795–827.
Van Roekel, L. P., & Maloney, E. D. (2012). Mixed layer modeling in the East Pacific warm pool during 2002. *Climate Dynamics*, *38*(11–12), 2559–2573.
VanZanten, M. C., Duynkerke, P. G., & Cuijpers, J. W. M. (1999). Entrainment parameterization in convective boundary layers. *Journal of the Atmospheric Sciences*, *56*(6), 813–828.
Vogelzang, D. H. P., & Holtslag, A. A. M. (1996). Evaluation and model impacts of alternative boundary-layer height formulations. *Boundary-Layer Meteorology*, *81*(3), 245–269.
Wang, D., McWilliams, J. C., & Large, W. G. (1998). Large-eddy simulation of the diurnal cycle of deep equatorial turbulence. *Journal of Physical Oceanography*, *28*(1), 129–148.
Whitt, D. B., & Taylor, J. R. (2017). Energetic submesoscales maintain strong mixed layer stratification during an autumn storm. *Journal of Physical Oceanography*, *47*(10), 2419–2427.
Zedler, S. E., Dickey, T. D., Doney, S. C., Price, J. F., Yu, X., & Mellor, G. L. (2002). Analyses and simulations of the upper ocean's response to Hurricane Felix at the Bermuda testbed Mooring site: 13–23 August 1995. *Journal of Geophysical Research*, *107*(C12), 25–1–25–29.